ARMY RESEARCH LABORATORY

Anisotropic Turbulence Models for Acoustic Propagation Through the Neutral Atmospheric Surface Layer

by David Keith Wilson

ARL-TR-1519 February 1998

Army Research Laboratory

Adelphi, MD 20783-1197

Anisotropic Turbulence Models for Acoustic Propagation Through the Neutral Atmospheric Surface Layer

David Keith Wilson
Information Science and Technology Directorate

Abstract

Several anisotropic models for the three-dimensional spectra of velocity fluctuations in shear-dominated, atmospheric surface-layer turbulence are presented and discussed. These models include a generalized Gaussian model, two forms of generalized von Kármán models; the Kristensen, Lenschow, Kirkegaard, and Courtney model; and the Mann model. The distinction between a "top-down" and "bottom-up" approach to the design of a model is discussed, and how the bottom-up approach generally leads to more satisfactory models is shown. The effects of turbulent anisotropy on acoustic propagation are explored by calculating mutual coherence functions (MCFs) (describing the coherence of a propagating acoustic wave) for the different models. Anisotropy effects have been found that they can be quite significant, even when the separation between the acoustic sensors is small.

Contents

iv

Figures

Tables

1. Introduction

Acoustical arrays can be used to determine the direction of a source. The principle is simple: through the use of phase differences across the array, the orientation of the incident wave fronts can be determined. If little refraction exists, the normals to the wave fronts correspond to the direction of the source. An important limiting factor in this process is the distortion of the propagating wave fronts caused by atmospheric turbulence. The turbulence introduces random perturbations to the wave fronts, so that they are no longer perfectly spherical waves radiating outward from the source (fig. 1). In such situations that the signal-to-noise ratio (SNR) is high, the turbulence effect is often the dominant factor affecting performance of the array (Wilson, 1997a).

The turbulence effect can be quantified by calculating the mutual coherence function (MCF), which describes the coherence between signals at a pair of sensors as a function of their spatial separation. The MCF for propagation through small-scale (inertial subrange) turbulence was determined long ago and has been applied successfully to optical and other types of wave propagation (see, for example, Tatarskii (1971)). Treatment of the inertial subrange is reasonably straight forward, primarily because the statistics of the small eddies are locally *isotropic* (independent of orientation) and *homogeneous* (independent of position). In the case of low-frequency acoustical propagation, however, large-scale (energy subrange) turbulence plays an important role. Hence it is necessary to account for such intrinsic features of the energy subrange as *anisotropy* and *inhomogeneity*. An example
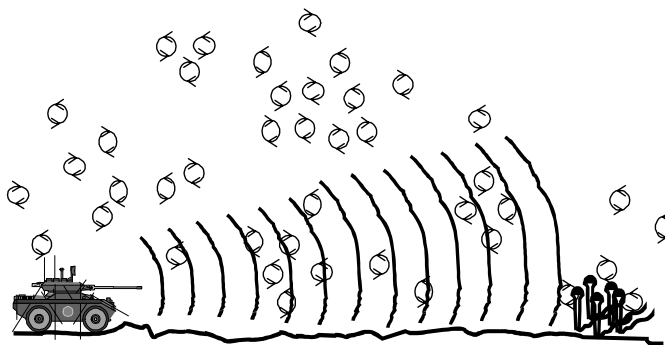
Figure 1. Random distortions in acoustic wave fronts caused by atmospheric turbulence.

of anisotropy is that the variance for turbulent velocity fluctuations in the direction of the mean wind is several times larger than the variance for vertical velocity fluctuations. An example of inhomogeneity is the dependence of the variances on the height above the ground. Similar manifestations of anisotropy and inhomogeneity are evident in the turbulent length scales.

In a previous report (Wilson, 1997b), I discussed a model for inhomogeneities in atmospheric turbulence that are introduced by "blocking" at the ground. This report is intended as a complement to the previous one. Its focus is on anisotropic models for atmospheric turbulence and on the implications for acoustic wave coherence as quantified by the MCF. As in the previous report, the turbulence models discussed are fully three-dimensional (3D), second-order statistical models. By this I mean that the models can be applied to any second-order statistic of the turbulence, with the orientations of the velocity components, as well as the direction of the spatial displacement between the two observation points, being arbitrary.

Although the turbulence models discussed in this report can be applied, in principle, to a broad range of atmospheric conditions, the selection of the model parameters described is for the specific case of a shear-driven, neutral, atmospheric surface layer. *Neutral*, in the terminology of geophysical fluid dynamics, means an absence of buoyant instabilities. Hence radiative heating and cooling of the ground (and the resulting temperature gradients in the overlying air) are neglected. This leaves *wind shear* as the dominant mechanism for generating the turbulence.

One of the points that is demonstrated in this report is that the modeling *procedure* becomes very important for anisotropic turbulence. If the procedure is ill-conceived, the result will often be a poor model that does not agree well with data and/or has parameters that are nearly impossible to determine. There are basically two possible procedures, which I call the "top-down approach" and the "bottom-up approach."[*] These approaches are illustrated in figure 2. The top-down approach has been used in the past to derive the popular isotropic von Kármán model. It begins by postulating an equation for the *specific turbulent kinetic energy (TKE) spectrum*[†] (just *energy spectrum* for short) of the turbulence, as was done in the previous report (Wilson, 1997b):

$$E\left(k\right) = \frac{4\Gamma\left(17/6\right)}{\sqrt{\pi}\Gamma\left(1/3\right)} \frac{\sigma^2 k^4 \ell^5}{\left(1 + k^2\ell^2\right)^{17/6}}. \tag{1}$$

---

[*]This usage of "top-down" and "bottom-up" should not be confused with the terminology coined for atmospheric boundary layer diffusion by Wyngaard and Brost (1984).

[†]*Specific* means per unit mass.
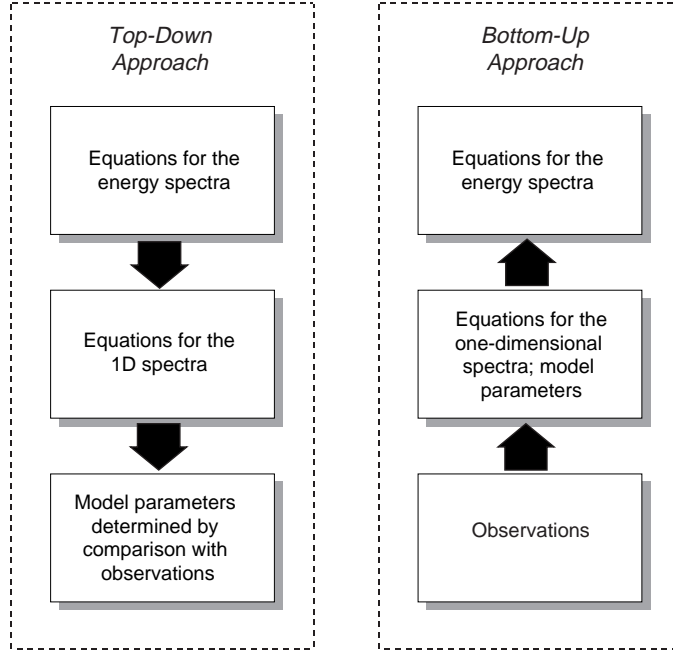
Figure 2. Two possible procedures for deriving statistical turbulence models.

The energy spectral equation has two unknown parameters, a length scale ℓ and a variance σ^2. (Other symbols and notation used in equation (1) are discussed in sect. 2 of this report.) When homogeneity and isotropy are assumed, a well-known set of relationships allows derivation of all other second-order statistical quantities, such as correlations and spectra, from the energy spectrum. For example, the one-dimensional (1D) spectrum, $F_L(k)$, which is measured by a stationary sensor when the fluid advects the turbulence past the sensor, is related to the energy spectrum through the equation (Batchelor, 1953)

$$E\left(k\right) = k^3 \frac{d}{dk}\left[\frac{1}{k}\frac{dF_L\left(k\right)}{dk}\right]. \tag{2}$$

It can be easily verified that

$$F_L\left(k\right) = \frac{4\Gamma\left(5/6\right)}{\sqrt{\pi}\Gamma\left(1/3\right)}\frac{\sigma^2\ell}{\left(1 + k^2\ell^2\right)^{5/6}}. \tag{3}$$

The key to determining the unknown parameters (ℓ and σ^2 in this case) is to derive one or more equations for observable quantities, such as $F_L(k)$. The parameters can then be deduced by fitting the derived equations to observations. The reason for calling this approach top-down is that the starting

point for the modeling procedure is the fundamental, underlying function: the energy spectrum.

The starting point in the second, or bottom-up, approach is the observed data. An equation for the 1D spectrum is then postulated, and its parameters are chosen according to the data. Then the more fundamental function, the energy spectrum, is determined in some manner from the 1D spectrum. This is the approach that has usually been adopted in the past to derive the popular, isotropic Gaussian model.

In the comparison of the top-down and bottom-up approaches, it is important to understand that the energy spectrum cannot be determined from the 1D spectrum without making some set of assumptions, such as homogeneity and isotropy, and then deriving a relationship such as equation (2). The process of determining the 1D spectrum from the energy spectrum is generally much more straight forward, involving integrations that are valid regardless of the turbulence properties.

For homogeneous and isotropic turbulence, the relationship between the energy spectrum and the 1D spectrum is so simple (eq (2)), it does not really matter whether one uses a top-down or bottom-up approach; it is easy to convert back and forth between the energy spectrum and the 1D spectrum. When anisotropy is considered, however, this conversion becomes *much* more difficult. Therefore some thought must be given to the distinction between the top-down and bottom-up approaches in the anisotropic case. We see, in fact, that although the top-down approach is more convenient from a mathematical standpoint, it is very difficult to derive a model agreeing well with observations when this approach is used. On the other hand, the bottom-up approach becomes mathematically cumbersome, although Kristensen *et al* (1989) have devised a systematic process for the derivation. The main reason for adopting the bottom-up approach is that it allows for creation of a model having good agreement with observations.

I consider six anisotropic models in this report. The reader may wonder why it is necessary to consider such a multitude. I am not suggesting that all of the models are, in the end, useful ones. Rather I introduce the large number of models in this report to document how anisotropic models can be developed from various starting points, and to compare their relative merits and fidelity to atmospheric measurements. By the time we finish, it should be clearer which models are actually worth retaining for future studies.

The first model I consider, a set of empirical equations owing to Kaimal *et al* (1972) (sect. 3), is actually valid only for 1D spectra, with the direction of the displacement along the axis of the mean wind. In this report, our main

use for Kaimal *et al*'s spectral equations is as a reference point for choosing parameters needed by the other, complete models derived in sections 4 to 7. For better or worse, the Kaimal *et al* equations are used as the "ground truth."

The second model I consider (sect. 4), which is original with this report, is essentially the top-down generalization of the popular anisotropic von Kármán model. The third model (sect. 5), also original with this report, is a bottom-up generalization of the anisotropic von Kármán model. The fourth model I consider (sect. 6) is due to Kristensen *et al* (1989). The Kristensen *et al* model is actually quite similar to the bottom-up anisotropic von Kármán one, although it is somewhat more complicated and flexible. The fifth model I consider is an anisotropic, bottom-up, generalization of the popular Gaussian model (sect. 7). The last model, the Mann (1994) model (sect. 8), is entirely different from the previous ones: it is a first-principle treatment for sheared turbulence. The Mann model is rather complex, but it contains certain realistic features of sheared turbulence that the other models do not capture. In section 9 of this report, example calculations of MCFs and source direction-finding performance for acoustical arrays are made using the various anisotropic turbulence models.

2. Preliminaries

This section reviews many of the basic correlation and spectral relationships involved in modeling of turbulence statistics and defines the notations used in subsequent sections of the report. It is assumed that the reader has a basic understanding of statistics and Fourier transformation.

The *correlation function tensor* is defined as

$$R_{ij}\left(\mathbf{x}, \mathbf{x} + \mathbf{r}\right) = \langle u_i\left(\mathbf{x}\right) u_j\left(\mathbf{x} + \mathbf{r}\right)\rangle, \tag{4}$$

where the angle brackets indicate ensemble averaging, and u_i and u_j are velocity fluctuations in the ith and jth directions. In this report, I follow the usual convention for orientation of the coordinates in micrometeorology: the x_1-axis is aligned with the direction of the mean wind (assumed horizontal), the x_2-axis is the horizontal axis perpendicular to the mean wind, and the x_3-axis is vertical.

In homogeneous turbulence (an assumption made throughout this report), the correlations depend only on the separation between the observation points:

$$R_{ij}\left(\mathbf{r}\right) = R_{ij}\left(\mathbf{x}, \mathbf{x} + \mathbf{r}\right). \tag{5}$$

The correlation function tensor forms a Fourier-transform pair with the *3D spectral density tensor* $\Phi_{ij}\left(\mathbf{k}\right)$:

$$R_{ij}\left(\mathbf{r}\right) = \int \Phi_{ij}\left(\mathbf{k}\right) \exp\left(i\mathbf{k} \cdot \mathbf{r}\right) d^3k, \tag{6}$$

$$\Phi_{ij}\left(\mathbf{k}\right) = \frac{1}{(2\pi)^3} \int R_{ij}\left(\mathbf{r}\right) \exp\left(-i\mathbf{k} \cdot \mathbf{r}\right) d^3r. \tag{7}$$

(The notation $\int d^3k$ in eq (6) means that the integration is to be carried out over the entire 3D **k**-space, and likewise **r**-space for eq (7).)

The covariance tensor is defined as

$$\sigma_{ij}^2 = \langle u_i\left(\mathbf{x}\right) u_j\left(\mathbf{x}\right)\rangle = R_{ij}\left(\mathbf{0}\right). \tag{8}$$

By evaluating equation (6) for $\mathbf{r} = \mathbf{0}$, we see that the covariance can also be found from the 3D spectral density by integrating over the wave number domain:

$$\sigma_{ij}^2 = \int \Phi_{ij}\left(\mathbf{k}\right) d^3k. \tag{9}$$

Normally in experiments the ***1D spectral density tensor*** $\Theta_{ij}(k)$ is measured. This quantity is defined as

$$\Theta_{ij,n}(k) = \frac{1}{2\pi} \int_{-\infty}^{\infty} R_{ij}(r\hat{\mathbf{e}}_n) \exp(-ikr)\ dr, \tag{10}$$

where $\hat{\mathbf{e}}_n$ is the unit vector along the x_n-axis. In the case of atmospheric turbulence, the measurement usually is performed from a stationary tower, and Taylor's hypothesis is invoked to convert the time series to a spatial one (Panofsky and Dutton, 1984). In this case, $\hat{\mathbf{e}}_n$ points in the direction of the mean wind.

Alternatively, we can determine the 1D spectral density from the 3D spectral density. Suppose we apply a 1D Fourier transform to equation (6) with respect to the x_n-axis and then evaluate the result with $\mathbf{r} = r\hat{\mathbf{e}}_n$. We find

$$\frac{1}{2\pi} \int_{-\infty}^{\infty} R_{ij}(r\hat{\mathbf{e}}_n) \exp(-ik_n r)\ dr = \int \Phi_{ij}(\mathbf{k})\ d^2 k_\perp, \tag{11}$$

where $\mathbf{k} = k_n\hat{\mathbf{e}}_n + \mathbf{k}_\perp$, $\mathbf{k}_\perp \equiv k_{\perp,1}\hat{\mathbf{e}}_{\perp,1} + k_{\perp,2}\hat{\mathbf{e}}_{\perp,2}$, and the subscripts "$\perp, m$" indicate the directions perpendicular to the x_n-axis. The left side of this equation is the same as the right side of equation (10), and so we have the result

$$\Theta_{ij,n}(k) = \int \Phi_{ij}(k\hat{\mathbf{e}}_n + \mathbf{k}_\perp)\ d^2 k_\perp. \tag{12}$$

For brevity, I often use $F_L(k)$, $F_T(k)$, and $F_V(k)$ in this report, instead of $\Theta_{11,1}(k)$, $\Theta_{22,1}(k)$, and $\Theta_{33,1}(k)$. This set of 1D autospectra, having the wave number vector aligned with the direction of the mean wind, is the one observable using a stationary sensor.

An important quantity in wave propagation is the ***two-dimensional (2D) correlation function*** $b_{ij,n}(\mathbf{r}_\perp)$:

$$b_{ij,n}(\mathbf{r}_\perp) = \frac{1}{2\pi} \int_{-\infty}^{\infty} R_{ij}(r_n\hat{\mathbf{e}}_n + \mathbf{r}_\perp)\ dr_n, \tag{13}$$

where $\mathbf{r}_\perp \equiv r_{\perp,1}\hat{\mathbf{e}}_{\perp,1} + r_{\perp,2}\hat{\mathbf{e}}_{\perp,2}$. In wave propagation problems, the x_n-axis is the direction of propagation, and usually only the wind components parallel to the direction of propagation are relevant. Hence $i = j = n$ is the main interest. A relationship between the 2D correlation and 3D spectral density can also be derived, by taking the 1D Fourier transform of equation (6) with respect to the x_n-axis, and then evaluating the result with $k_n = 0$. We find

$$b_{ij,n}(\mathbf{r}_\perp) = \int \Phi_{ij}(\mathbf{k}_\perp) \exp(i\mathbf{k}_\perp \cdot \mathbf{r}_\perp)\ d^2 k_\perp. \tag{14}$$

In the context of wave propagation, it is also useful to define a 2D structure function $d_{ij,n}(\mathbf{r}_\perp)$ as

$$d_{ij,n}(\mathbf{r}_\perp) = 2\left[b_{ij,n}(\mathbf{0}) - b_{ij,n}(\mathbf{r}_\perp)\right]. \tag{15}$$

The 2D structure function is the 2D counterpart of the usual (3D) structure function encountered in turbulence theory.

We define the integral length scale as

$$L_{ij,n} = \frac{1}{\sigma_{ij}^2} \int_0^\infty R_{ij}(r\hat{\mathbf{e}}_n)\, dr. \tag{16}$$

Various useful relationships between the integral length scale, the spectral densities, and the 2D correlation function can be derived from the Fourier transform relations. First note that when $i = j$, the correlation function is an even function and equation (16) can be rewritten

$$L_{ii,n} = \frac{1}{2\sigma_{ii}^2} \int_{-\infty}^\infty R_{ii}(r\hat{\mathbf{e}}_n)\, dr.$$

By taking the 1D Fourier transform of equation (6) with respect to the x_n-axis, and then evaluating the result with $k_n = 0$ and $\mathbf{r}_\perp = \mathbf{0}$, it can be shown that

$$L_{ii,n} = \frac{\pi}{\sigma_{ii}^2} \int \Phi_{ii}(\mathbf{k}_\perp)\, d^2 k_\perp. \tag{17}$$

By setting $k = 0$ in equation (12), we therefore have

$$L_{ii,n} = \frac{\pi}{\sigma_{ii}^2}\, \Theta_{ii,n}(0). \tag{18}$$

Furthermore, by setting $\mathbf{r}_\perp = \mathbf{0}$ in equation (14), we have

$$L_{ii,n} = \frac{\pi}{\sigma_{ii}^2}\, b_{ii,n}(\mathbf{0}). \tag{19}$$

3.   Kaimal *et al* Model

Kaimal *et al* (1972) developed a simple set of empirical formulas for the 1D velocity spectra. Their equations are actually for the *frequency*, rather than the *wave number*, spectra, such as discussed in section 2. With the assumption of Taylor's hypothesis though (which states that the turbulence is "frozen" as it moves past the sensor at the mean wind speed U), their frequency n is simply equal to $Uk/2\pi$. As a result Kaimal *et al*'s equations 21a to 21b for the spectra of the horizontal velocity components become, in the notation of this report,

$$F_L\left(k\right) = \Theta_{11,1}\left(k\right) = \frac{b_1 z u_*^2}{4\pi\left(1 + c_1\left|k\right| z/2\pi\right)^{5/3}}, \tag{20}$$

$$F_T\left(k\right) = \Theta_{22,1}\left(k\right) = \frac{b_2 z u_*^2}{4\pi\left(1 + c_2\left|k\right| z/2\pi\right)^{5/3}}, \tag{21}$$

where $b_1 = 105$, $c_1 = 33$, $b_2 = 17$, and $c_2 = 9.5$. The equation for the vertical velocity spectrum is

$$F_V\left(k\right) = \Theta_{33,1}\left(k\right) = \frac{b_3 z u_*^2}{4\pi\left[1 + c_3\left(\left|k\right| z/2\pi\right)^{5/3}\right]}, \tag{22}$$

where $b_3 = 2$ and $c_3 = 5.3$. Kaimal *et al*'s equations are plotted in figures 3 to 5.

Kaimal *et al*'s equations, since they describe only the 1D spectra, do not constitute a complete 3D model for anisotropic turbulence. However, in the remainder of this report, they are used frequently as a reference point. They are compared to the various complete models that are developed further on, and the parameters in the complete models (such as variances and length scales) are chosen to produce a good agreement with Kaimal *et al*'s equations.

The variances corresponding to the Kaimal *et al* spectra can be found by integrating the spectra from $k = -\infty$ to ∞ (eq (1)). The result for the horizontal velocity components is

$$\sigma_{ii}^2 = \frac{3 b_i u_*^2}{2 c_i}.$$

9
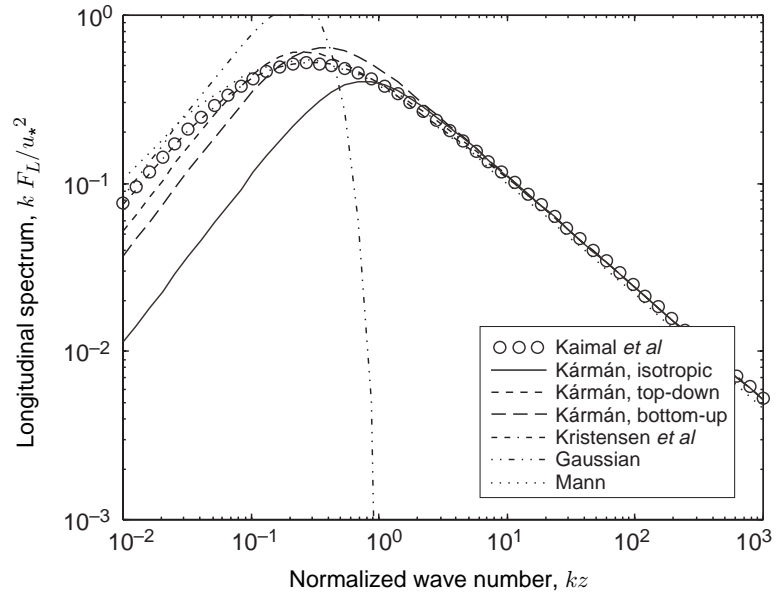
Figure 3. One-dimensional turbulence spectra for streamwise (longitudinal) velocity fluctuations.
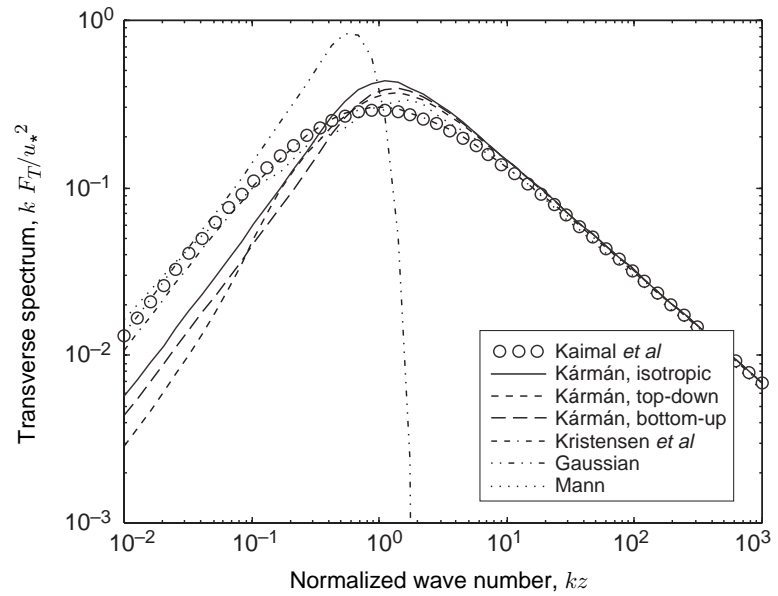
Figure 4. One-dimensional turbulence spectra for horizontal, cross-stream (lateral) velocity fluctuations.

10

For the vertical velocity,

$$\sigma_{33}^2 = \frac{3\pi b_3 u_*^2}{5\sin\left(2\pi/5\right) c_3^{3/5}}$$

The computed values for the variances are shown in table 1.

The integral length scales can be determined easily using equation (18). We find

$$L_{ii,1} = \frac{b_i z u_*^2}{4\sigma_{ii}^2}.$$

The resulting values for the integral length scales are also shown in table 1.
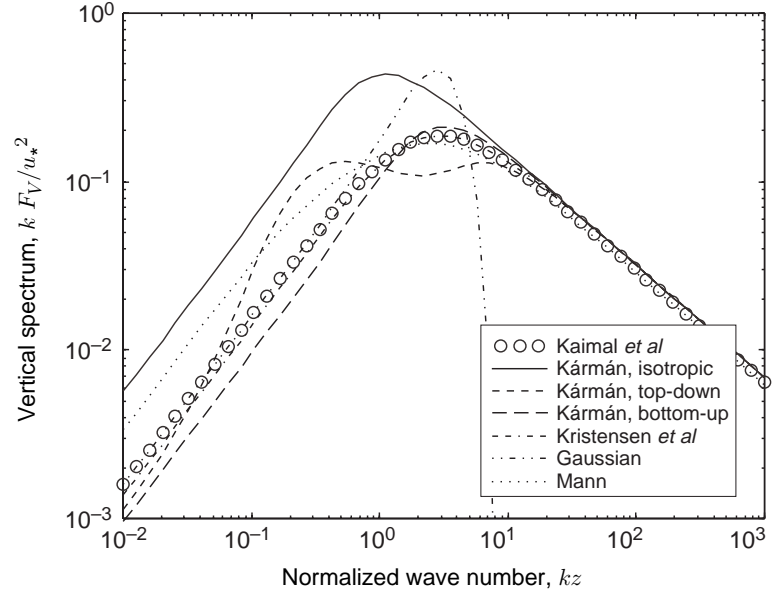
Figure 5. One-dimensional turbulence spectra for vertical velocity fluctuations.

Table 1. Values for variances σ_{ii}^2 and streamwise integral length scales $L_{ii,1}$ corresponding to Kaimal model.

i	σ_{ii}^2	$L_{ii,1}$
1	$4.77u_*^2$	$5.50z$
2	$2.68u_*^2$	$1.59z$
3	$1.46u_*^2$	$0.343z$

4. Von Kármán-Based Anisotropic Model, Top-Down Approach

In this section, I attempt to develop a model for anisotropic turbulence using a top-down approach. The model equations are based upon those used for the popular isotropic von Kármán model.

4.1 Anisotropic Spectral Density Tensor

Kristensen *et al* (1989) have proposed the following equation for the 3D spectra in anisotropic turbulence:

$$\Phi_{ij}(\mathbf{k}) = \sum_{m=1}^{3} A_m(k) \left(\delta_{mi} - \frac{k_m k_i}{k^2} \right) \left(\delta_{mj} - \frac{k_m k_j}{k^2} \right). \tag{23}$$

Their equation satisfies the incompressibility condition for the turbulence. Note that when $A_1(k) = A_2(k) = A_3(k) \equiv A(k)$, the equation reduces to the familiar equation for isotropic turbulence (e.g., Batchelor, 1953)

$$\Phi_{ij}(\mathbf{k}) = \frac{E(k)}{4\pi k^2} \left(\delta_{ij} - \frac{k_i k_j}{k^2} \right), \tag{24}$$

where

$$A(k) = \frac{E(k)}{4\pi k^2}, \tag{25}$$

and $E(k)$ is the energy spectrum for turbulent kinetic energy (TKE).

An important point regarding equation (23) is that it is only an *idealized* form for the 3D spectra in anisotropic, homogeneous turbulence. In devising it, Kristensen *et al* neglected many of the assymetries that are possible in anisotropic turbulence. For example, equation (23) has the symmetry property $\Phi_{13}(k_1, k_2, k_3) = -\Phi_{13}(k_1, k_2, -k_3)$. Hence when Φ_{13} is integrated from $k_3 = -\infty$ to ∞, the result is zero. This implies that the 1D spectrum $\Theta_{13,1}(k)$ is zero for all k (see eq (12)) and therefore also that the covariance $\langle u_1 u_3 \rangle$ is zero. But negative $\langle u_1 u_3 \rangle$ is a fundamental characteristic of a shear layer, since there is a transfer of streamwise momentum toward the surface. Despite such inherent shortcomings, equation (23) is used to develop most of the anisotropic turbulence models in the remainder of this report. It is just a first step toward creating turbulence models with realistic

anisotropy; we will see that even this simple first step causes very significant additional complications. In section 8, I consider an altogether different model, the Mann model, that does break away from the constraints of equation (23), predicting a negative value for $\langle u_1 u_3 \rangle$.

The basic idea of the top-down approach is that we build our turbulence model from equations for the energy spectra. When the turbulence is isotropic, a flexible and useful form for the energy spectrum is

$$E\left(k\right) \;=\; \frac{3}{B\left[\left(\mu+1\right)/2,\nu\right]} \frac{\sigma^2 \ell \left(k\ell\right)^{\mu}}{\left(1+k^2\ell^2\right)^{\left(\mu+1\right)/2+\nu}}, \tag{26}$$

where

$$B\left(x,y\right) \;=\; \frac{\Gamma\left(x\right)\Gamma\left(y\right)}{\Gamma\left(x+y\right)} \tag{27}$$

is called the beta function, and $\Gamma\left(\cdot\right)$ is the gamma function. The reader can verify, using equation (A-1), that integration of this energy spectrum from $k = 0$ to $k = \infty$ yields $3\sigma^2/2$ for all values of μ and ν. Hence σ^2 is the variance of a single velocity component. The parameter μ controls the slope of the spectrum in the energy subrange, $k\ell \gg 1$, where $E\left(k\right) \propto k^{\mu}$. For the inertial subrange, $k\ell \gg 1$, $E\left(k\right) \propto k^{-1-2\nu}$.

What is classically called the ***von Kármán model*** corresponds to $\mu = 4$, and $\nu = 1/3$. This value for ν produces an inertial-subrange spectrum proportional to $k^{-5/3}$, in agreement with Kolmogorov's scaling arguments for this part of the spectrum (Kolmogorov, 1941). The classical von Kármán energy spectrum was given earlier as equation (1).

In this paper, I assume that the $A_i\left(k\right)$ each have $\mu = 6$ and $\nu = 1/3$. The reason for choosing $\mu = 6$ is simply that this value allowed quantities such as the 1D spectral densities to be derived in analytical form, whereas $\mu = 4$ did not. (Actually, any value $\mu = 2n$, where $n \geq 3$, will work.) Given these assumptions, our equation for $A_i\left(k\right)$ is

$$A_i\left(k\right) = \frac{3}{4\pi B\left(7/2,1/3\right)} \frac{a_i k^4 \ell_i^7}{\left(1+k^2\ell_i^2\right)^{23/6}}. \tag{28}$$

In this report, I call this turbulence model, based entirely on equations (23) and (28), the ***top-down anisotropic von Kármán model.***

Note that six parameters are in this version of the anisotropic von Kármán model. However, since the inertial subrange must be isotropic, we require for $k\ell_i \gg 1$ that

$$A_1\left(k\right) = A_2\left(k\right) = A_3\left(k\right).$$

As a result we must have

$$a_1 \ell_1^{-2/3} = a_2 \ell_2^{-2/3} = a_3 \ell_3^{-2/3}. \tag{29}$$

Let us define

$$\sigma^2 = \frac{a_1 + a_2 + a_3}{3}, \tag{30}$$

and

$$\ell^{2/3} = \frac{\ell_1^{2/3} + \ell_2^{2/3} + \ell_3^{2/3}}{3}. \tag{31}$$

It can then be shown that

$$\sigma^2 \ell^{-2/3} = a_i \ell_i^{-2/3}, \; i = 1, 2, 3. \tag{32}$$

This relationship will be useful later in this section.

The anisotropic energy spectra for the top-down von Kármán model are plotted in figures 6 to 8. The parameters used for these curves were chosen by methods to be discussed in section 4.5. As one would expect, the A_i's for the top-down von Kármán model have a smooth, single peak, reminiscent of the isotropic von Kármán energy spectrum. In comparison to the isotropic von Kármán model[*] (also shown in the figures), the anisotropic version of A_1 peaks at a higher wave number, whereas A_3 peaks at a lower wave number. The peaks for A_2 roughly coincide.
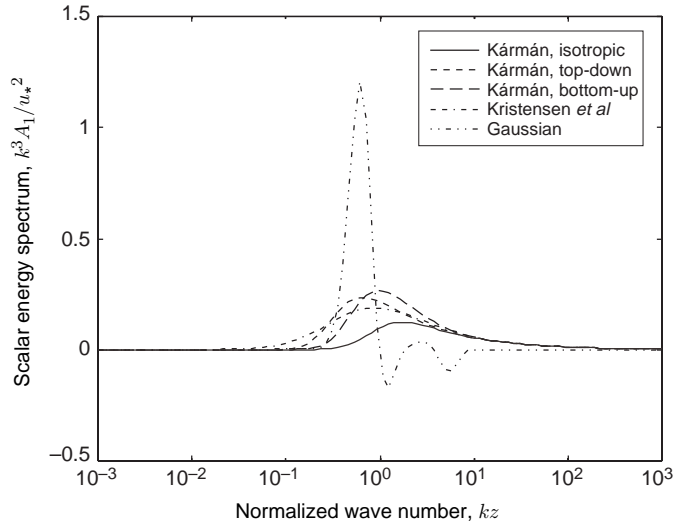
Figure 6. Anisotropic energy spectra for longitudinal velocity component.

---

[*]Equations for the isotropic von Kármán model appear in Wilson (1997a).

14
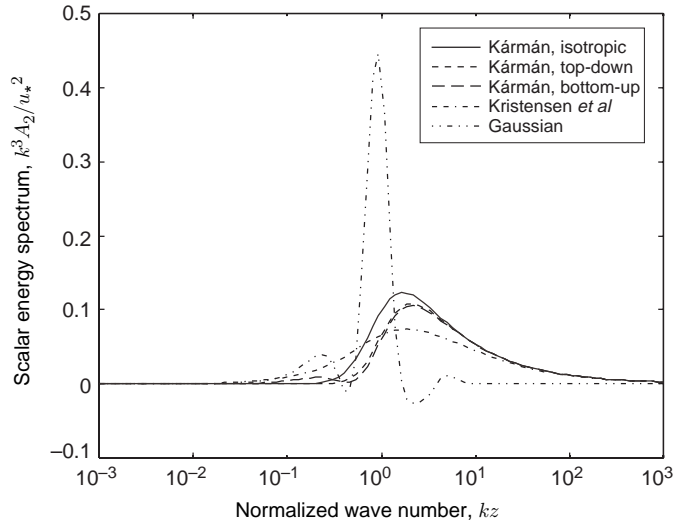
Figure 7. Anisotropic energy spectra for lateral velocity component.
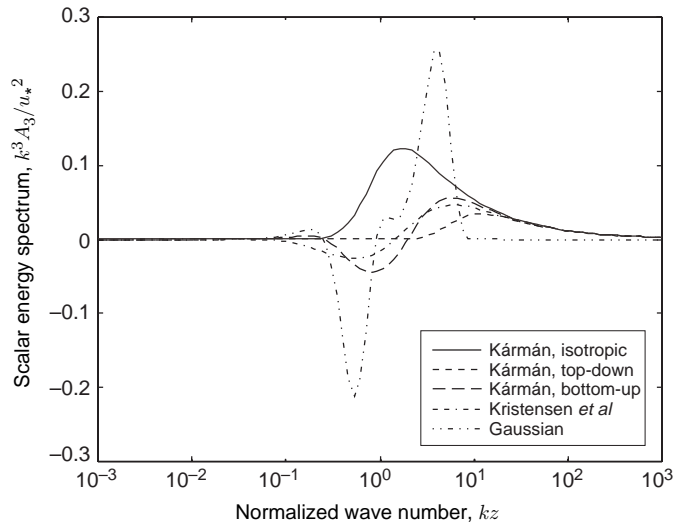
Figure 8. Anisotropic energy spectra for vertical velocity component.

15

4.2 Variances

With the use of equation (23), the spectrum $\Phi_{11}\left(\mathbf{k}\right)$ is given by

$$\Phi_{11}\left(\mathbf{k}\right) = A_1\left(k\right)\left(1 - \frac{k_1^2}{k^2}\right)^2 + A_2\left(k\right)\left(-\frac{k_1 k_2}{k^2}\right)^2 + A_3\left(k\right)\left(-\frac{k_1 k_3}{k^2}\right)^2. \tag{33}$$

To find the variance, we need to calculate the integral

$$\sigma_{11}^2 = \int \Phi_{11}\left(\mathbf{k}\right)\,d\mathbf{k}.$$

In spherical coordinates ($k_1 = k\cos\theta\sin\phi$, $k_2 = k\sin\theta\sin\phi$, $k_3 = k\cos\phi$), the integral becomes

$$\sigma_{11}^2 = \int_0^\infty \int_0^\pi \int_0^{2\pi} \left[A_1\left(k\right)\left(1 - \cos^2\theta\sin^2\phi\right)^2 + A_2\left(k\right)\left(\cos\theta\sin\theta\sin^2\phi\right)^2 \right.$$
$$\left. + \; A_3\left(k\right)\left(\cos\theta\sin\phi\cos\phi\right)^2\right]k^2\sin\phi\,d\theta\,d\phi\,dk.$$

Performing the integrations over θ and ϕ yields

$$\sigma_{11}^2 = \frac{4\pi}{15}\int_0^\infty \left[8A_1\left(k\right) + A_2\left(k\right) + A_3\left(k\right)\right]k^2\,dk.$$

Substituting with equation (28) and evaluating the resulting integrals using equation (A-1), we find

$$\sigma_{11}^2 = \frac{1}{10}\left(8a_1 + a_2 + a_3\right). \tag{34}$$

Similarly, it can be shown that

$$\sigma_{22}^2 = \frac{1}{10}\left(a_1 + 8a_2 + a_3\right), \tag{35}$$

$$\sigma_{33}^2 = \frac{1}{10}\left(a_1 + a_2 + 8a_3\right). \tag{36}$$

4.3   1D Spectral Densities

First let us consider the case in which $i = j = n$ in equation (12). Setting $k_2 = k_\perp\cos\theta$ and $k_3 = k_\perp\sin\theta$ in equation (33), we find

$$\Phi_{11}\left(\mathbf{k}\right) = A_1\left(k\right)\frac{k_\perp^4}{k^4} + A_2\left(k\right)\frac{k_1^2 k_\perp^2\cos^2\theta}{k^4} + A_3\left(k\right)\frac{k_1^2 k_\perp^2\sin^2\theta}{k^4}. \tag{37}$$

After converting equation (12) to cylindrical coordinates and performing the integration over θ, we have

$$\Theta_{11,1}\left(k_1\right) = 2\pi\int_0^\infty \left[k_\perp^2 A_1\left(k\right) + \frac{1}{2}k_1^2 A_2\left(k\right) + \frac{1}{2}k_1^2 A_3\left(k\right)\right]\frac{k_\perp^3}{k^4}\,dk_\perp. \tag{38}$$

16

When $A_i(k)$ is given by equation (28), the terms in equation (38) can be easily integrated using equation (A-2). The result is

$$F_L(k) = \frac{1}{B(1/2, 1/3)} \left[\frac{4a_1\ell_1}{5\left(1 + k^2\ell_1^2\right)^{5/6}} + \frac{a_2 k^2 \ell_2^3}{6\left(1 + k^2\ell_2^2\right)^{11/6}} + \frac{a_3 k^2 \ell_3^3}{6\left(1 + k^2\ell_3^2\right)^{11/6}} \right]. \tag{39}$$

Next let us find an expression for $\Theta_{22,1}(k)$. First note, from equation (23), that $\Phi_{22}(\mathbf{k})$ can be written

$$\begin{aligned}
\Phi_{22}(\mathbf{k}) &= A_1(k) \frac{k_1^2 k_\perp^2 \cos^2\theta}{k^4} + A_2(k) \frac{k_1^4 + 2k_1^2 k_\perp^2 \sin^2\theta + k_\perp^4 \sin^4\theta}{k^4} \\
&\quad + A_3(k) \frac{k_\perp^4\left(\cos^2\theta - \cos^4\theta\right)}{k^4}.
\end{aligned} \tag{40}$$

Integrating with respect to θ, we find

$$\Theta_{22,1}(k_1) = 2\pi \int_0^\infty \left[\frac{1}{2} k_1^2 k_\perp^2 A_1(k) + \left(k_1^4 + k_1^2 k_\perp^2 + \frac{3}{8} k_\perp^4 \right) A_2(k) + \frac{1}{8} k_\perp^4 A_3(k) \right] \frac{k_\perp}{k^4} \, dk_\perp. \tag{41}$$

The result of the integration over $k_\perp$ is

$$\begin{aligned}
F_T(k) &= \frac{1}{B(1/2, 2/3)} \left[\frac{a_1 k^2 \ell_1^3}{6\left(1 + k^2\ell_1^2\right)^{11/6}} + \frac{3a_2 \ell_2}{10\left(1 + k^2\ell_2^2\right)^{5/6}} \right. \\
&\quad \left. + \frac{a_2 k^2 \ell_2^3}{3\left(1 + k^2\ell_2^2\right)^{11/6}} + \frac{11a_2 k^4 \ell_2^5}{18\left(1 + k^2\ell_2^2\right)^{17/6}} + \frac{a_3 \ell_3}{10\left(1 + k^2\ell_3^2\right)^{5/6}} \right].
\end{aligned} \tag{42}$$

Similarly,

$$\begin{aligned}
F_V(k) &= \frac{1}{B(1/2, 2/3)} \left[\frac{a_1 k^2 \ell_1^3}{6\left(1 + k^2\ell_1^2\right)^{11/6}} + \frac{a_2 \ell_2}{10\left(1 + k^2\ell_2^2\right)^{5/6}} \right. \\
&\quad \left. + \frac{3a_3 \ell_3}{10\left(1 + k^2\ell_3^2\right)^{5/6}} + \frac{a_3 k^2 \ell_3^3}{3\left(1 + k^2\ell_3^2\right)^{11/6}} + \frac{11a_3 k^4 \ell_3^5}{18\left(1 + k^2\ell_3^2\right)^{17/6}} \right].
\end{aligned} \tag{43}$$

In the inertial subrange ($k\ell_i \gg 1$), it is widely known that the 1D spectra satisfy isotropy and are proportional to $k^{-5/3}$. (This was originally suggested by Kolmogorov (1941).) In the inertial subrange, equations (39) and (42) reduce to

$$\begin{aligned}
\Theta_{11,1}\left(k\right) &\cong \frac{1}{B\left(1/2,1/3\right)}\left(\frac{4}{5}a_1\ell_1^{-2/3}+\frac{1}{6}a_2\ell_2^{-2/3}+\frac{1}{6}a_3\ell_3^{-2/3}\right)k^{-5/3}\\
&=\frac{17}{15B\left(1/2,1/3\right)}\sigma^2\ell^{-2/3}k^{-5/3},
\end{aligned}$$

and

$$\begin{aligned}
\Theta_{22,1}\left(k\right) &\cong \frac{1}{B\left(1/2,1/3\right)}\left(\frac{1}{6}a_1\ell_1^{-2/3}+\frac{56}{45}a_2\ell_2^{-2/3}+\frac{1}{10}a_3\ell_3^{-2/3}\right)k^{-5/3}\\
&=\frac{68}{45B\left(1/2,1/3\right)}\sigma^2\ell^{-2/3}k^{-5/3}.
\end{aligned}$$

(Eq (32) was used in deriving the equations above.) Note that both spectra have the proper $k^{-5/3}$ dependence. Furthermore, the ratio $\Theta_{11,1}\left(k\right)/\Theta_{22,1}\left(k\right)$ equals $4/3$, another well-known result for the inertial subrange (Panofsky and Dutton, 1984).

The 1D spectra for the top-down von Kármán model are compared to Kaimal *et al*'s equations in figures 3 to 5. In making these plots, I selected the parameters in the manner to be discussed in section 4.5. Agreement is fairly good for the streamwise spectrum F_L. The peak in the von Kármán model is somewhat sharper, and the spectral levels for small kz are lower. Similar comments apply to the cross-stream spectrum, F_T, with the mismatch for small kz being even more severe. The vertical spectrum F_V is rather peculiar. It has two peaks, one at $kz \sim 0.3$, and the second at $kz \sim 10$. This behavior is quite unphysical and does not agree well with the Kaimal *et al*'s spectra. The behavior is an unfortunate difficulty with the top-down approach to modeling the anisotropic spectra: it can result in multiple-peaked 1D spectra.

4.4 2D Correlation Functions

From equation (23), we see that

$$\Phi_{11}\left(0,k_2,k_3\right)=A_1\left(k_\perp\right),\tag{44}$$

where $k_\perp^2 = k_2^2 + k_3^2$. Hence equation (14) reduces to

$$b_{11,1}\left(\mathbf{r}_\perp\right)=\int A_1\left(k_\perp\right)\exp\left(i\mathbf{k}_\perp\cdot\mathbf{r}_\perp\right)d^2k_\perp.\tag{45}$$

Rewriting the integral in cylindrical coordinates and performing the integration over angle, we have

$$b_{11,1}\left(r_\perp\right)=2\pi\int_0^\infty A_1\left(k_\perp\right)J_0\left(k_\perp r_\perp\right)k_\perp\,dk_\perp,\tag{46}$$

where $J_\nu(\cdot)$ is the Bessel function of the first kind.

Now, substituting equation (28) into equation (46), we have

$$b_{11,1}(r_\perp) = \frac{3a_1}{2B(7/2, 1/3)} \int_0^\infty \frac{k_\perp^5 \ell_1^7}{(1 + k_\perp^2 \ell_1^2)^{23/6}} J_0(k_\perp r_\perp)\, dk_\perp. \quad (47)$$

To perform the integrations, we can use the recurrence formula for Bessel functions

$$J_{n+1}(x) = \frac{2n}{x} J_n(x) - J_{n-1}(x).$$

Hence

$$k_\perp^5 J_0(k_\perp r_\perp) = \frac{8k_\perp^3}{r_\perp^2} J_2(k_\perp r_\perp) - \frac{8k_\perp^4}{r_\perp} J_3(k_\perp r_\perp) + k_\perp^5 J_4(k_\perp r_\perp).$$

Now the integration over $k_\perp$ can be accomplished using equation (A-3). The result is

$$b_{11,1}(r_\perp) = \frac{4a_1 \ell_1}{5\sqrt{\pi}\Gamma(1/3)} \left(\frac{r_\perp}{2\ell_1}\right)^{17/6} \left[\frac{8\ell_1^2}{r_\perp^2} K_{5/6}\left(\frac{r_\perp}{\ell_1}\right) - \frac{8\ell_1}{r_\perp} K_{1/6}\left(\frac{r_\perp}{\ell_1}\right) + K_{7/6}\left(\frac{r_\perp}{\ell_1}\right)\right], \quad (48)$$

where $K_\nu(\cdot)$ is the modified Bessel function of the second kind. The formula for $b_{22,2}(r_\perp)$ is the same, except with a_2 replacing a_1, and ℓ_2 replacing ℓ_1.

To find the approximate form of the 2D correlation for small separations $(r_\perp/\ell \ll 1)$, we use the following series expansion for the Bessel functions:

$$K_\nu(\xi) \simeq \frac{\Gamma(\nu)}{2} \left(\frac{\xi}{2}\right)^{-\nu} - \frac{\Gamma(1-\nu)}{2\nu} \left(\frac{\xi}{2}\right)^{\nu} + \frac{\Gamma(\nu)}{2(1-\nu)} \left(\frac{\xi}{2}\right)^{2-\nu}. \quad (49)$$

The result of substituting this series into equation (48) is

$$b_{11,1}(r_\perp) \simeq \frac{4\Gamma(5/6)a_1\ell_1}{5\sqrt{\pi}\Gamma(1/3)} \left[1 - \frac{187\Gamma(1/6)}{60\Gamma(5/6)} \left(\frac{r_\perp}{2\ell_1}\right)^{5/3} + 18\left(\frac{r_\perp}{2\ell_1}\right)^2\right]. \quad (50)$$

Hence the 2D structure function, equation (15), is

$$d_{11,1}(r_\perp) \simeq \frac{11\Gamma(1/6)}{30\sqrt{\pi}\Gamma(2/3)} C_u^2 r_\perp^{5/3} - \frac{36\Gamma(5/6)a_1\ell_1}{5\sqrt{\pi}\Gamma(1/3)} \left(\frac{r_\perp}{\ell_1}\right)^2, \quad (51)$$

where

$$C_u^2 = \frac{34\sigma^2\Gamma(2/3)}{5\Gamma(1/3)} (2\ell)^{-2/3} \quad (52)$$

is the structure-function parameter. The first term in equation (51) is the one for isotropic, inertial-subrange turbulence. It is the most important term for

very small $r_\perp$. But as $r_\perp$ approaches ℓ and ℓ_1, the other terms quickly become important. Hence inertial-subrange approximations for the 2D structure function generally are unsatisfactory.

Note that the 2D structure functions for the top-down anisotropic von Kármán model are independent of the direction of the displacement. This is, in fact, a consequence of using the simplified form of anisotropy implied by equation (23). It is **not** a general feature of anisotropic turbulence. On the other hand, the model predictions **do** depend on the orientation of the velocity fluctuations. For example, $d_{11,1}(r_\perp) \neq d_{22,2}(r_\perp)$.

The 2D structure function for the along-wind direction ($d_{11,1}(r_\perp)$) for the top-down anisotropic von Kármán model is plotted in figure 9. The corresponding structure function for crosswind direction ($d_{22,2}(r_\perp)$) is plotted in figure 10. These predictions were made using the parameter selections discussed in section 4.5. The model predicts that the 2D structure function is larger in along-wind direction than in the crosswind direction. This is to be expected, since the variance of the along-wind velocity fluctuations is higher than for the crosswind fluctuations.

4.5 Parameter Selection

In this section, I determine the parameters by forcing the anisotropic von Kármán model to have the same variances and TKE dissipation rates as the empirical equations developed by Kaimal *et al* (1972). First let us consider
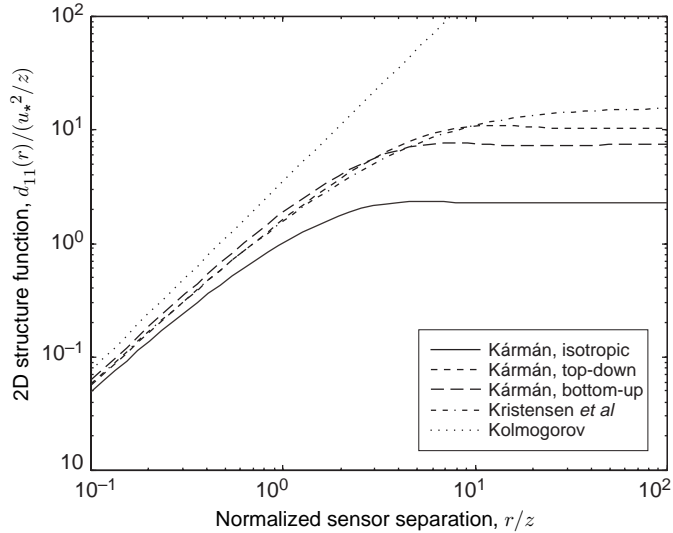
Figure 9. Predictions of 2D structure function for along-wind direction, for Kologorov model, various von Kármán models, and Kristensen *et al* model.
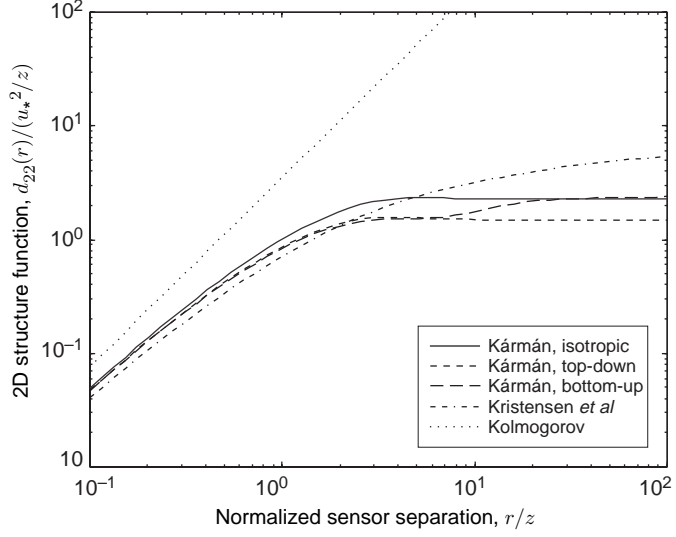
Figure 10. Predictions of 2D structure function for crosswind direction, for Kolmogorov model, various von Kármán models, and Kristensen *et al* model.

the variances. By comparing equations (34) to (36) to table 1, we have the following matrix equation:

$$
\begin{bmatrix} 0.8 & 0.1 & 0.1 \\ 0.1 & 0.8 & 0.1 \\ 0.1 & 0.1 & 0.8 \end{bmatrix} \begin{bmatrix} a_1 \\ a_2 \\ a_3 \end{bmatrix} = \begin{bmatrix} 4.77 \\ 2.68 \\ 1.46 \end{bmatrix} u_*^2.
$$

Solving this system yields the values for the a_i's shown in table 2.

The parameters ℓ_i can be determined by matching the TKE dissipation rate in the inertial subrange. For $k\ell_1 \gg 1$, equation (39) becomes

$$
\Theta_{11,1}(k) \cong \frac{17}{15B(1/2,1/3)} a_1 \ell_1^{-2/3} k^{-5/3}.
$$

But Kaimal *et al* (1972) have demonstrated the following equation

$$
\Theta_{11,1}(k) \cong \frac{\alpha_1}{2} \epsilon^{2/3} k^{-5/3}, \tag{53}
$$

where ϵ is the TKE dissipation rate, and α_1 is a constant approximately equal to 0.56 (Kaimal *et al*, 1972, Kristensen *et al*, 1989). Therefore

$$
\frac{17}{15B(1/2,1/3)} \sigma^2 \ell^{-2/3} = \frac{\alpha_1}{2} \epsilon^{2/3}. \tag{54}
$$

21

Table 2. Values for top-down von Kármán model parameters a_i and ℓ_i.

i	a_i	ℓ_i
1	$5.54u_*^2$	$4.92z$
2	$2.56u_*^2$	$1.54z$
3	$0.813u_*^2$	$0.277z$

It can be shown that the TKE dissipation rate in a neutral shear layer is

$$\epsilon = \frac{u_*^3}{\kappa z}, \tag{55}$$

where u_* is called the *friction velocity*, z is the height from the ground, and $\kappa \simeq 0.4$ is called **von Kármán's constant** (Stull, 1988). Solving equation (54) for ℓ, we have

$$\ell_1 = \left[\frac{34a_1}{15\alpha_1 B\left(1/2, 1/3\right)} \right]^{3/2} \frac{\kappa z}{u_*^3} \simeq 0.378 \frac{a_1^{3/2} z}{u_*^3} \simeq 4.92z. \tag{56}$$

The parameters ℓ_2 and ℓ_3 now follow easily from equation (29). The resulting values for the ℓ_i are shown in table 2.

5. Von Kármán-Based Anisotropic Model, Bottom-Up Approach

Since our initial attempt to derive a simple anisotropic von Kármán model was not very successful in producing 1D spectra that agree well with data (sect. 4), we try in this section a second approach similar to the one devised by Kristensen *et al* (1989). The idea is to use the same set of equations for the 1D spectra as in the isotropic von Kármán model (although with different parameters), so that the isotropic and anisotropic versions match when the variances and length scales are all equal.

5.1   1D Spectral Densities

Let us assume the 1D longitudinal spectrum has the form

$$F_L(k) = \Theta_{11,1}(k) = \frac{1}{B(1/2, 1/3)} \frac{\sigma_{11}^2 \ell_1}{\left(1 + k^2 \ell_1^2\right)^{5/6}}. \tag{57}$$

In isotropic turbulence,

$$F_T(k) = F_V(k) = \frac{1}{2}\left[F_L(k) - kF_L'(k)\right]. \tag{58}$$

Since

$$F_L(k) - kF_L'(k) = \frac{1}{B(1/2, 1/3)} \frac{\sigma_{11}^2 \ell_1}{\left(1 + k^2 \ell_1^2\right)^{5/6}}\left(1 + \frac{5}{3}\frac{k^2 \ell_1^2}{1 + k^2 \ell_1^2}\right),$$

natural choices for $F_T(k)$ and $F_V(k)$ are

$$F_T(k) = \Theta_{22,1}(k) = \frac{1}{2B(1/2, 1/3)} \frac{\sigma_{22}^2 \ell_2}{\left(1 + k^2 \ell_2^2\right)^{5/6}}\left(1 + \frac{5}{3}\frac{k^2 \ell_2^2}{1 + k^2 \ell_2^2}\right), \tag{59}$$

and

$$F_V(k) = \Theta_{33,1}(k) = \frac{1}{2B(1/2, 1/3)} \frac{\sigma_{33}^2 \ell_3}{\left(1 + k^2 \ell_3^2\right)^{5/6}}\left(1 + \frac{5}{3}\frac{k^2 \ell_3^2}{1 + k^2 \ell_3^2}\right). \tag{60}$$

When the variances and length scales are all equal, equation (57) reduces to equation (18) in Wilson (1997b), which gives the longitudinal, 1D spectrum for the isotropic von Kármán model. Equations (59) and (60) reduce to

equation (27) in the Wilson report, which gives the transverse, 1D spectrum in the isotropic von Kármán model. If we define

$$F_0\left(\sigma, \ell, a, \nu; k\right) = \frac{\sigma^2 \ell}{B\left(1/2, \nu\right)} \frac{1}{\left(1 + k^2 \ell^2\right)^{\nu + 1/2}} \left(1 + \frac{a k^2 \ell^2}{1 + k^2 \ell^2}\right), \qquad (61)$$

we can conveniently state equations (57) to (60) as

$$F_L\left(k\right) = F_0\left(\sigma_{11}, \ell_1, 0, 1/3; k\right), \qquad (62)$$

$$F_T\left(k\right) = \frac{1}{2} F_0\left(\sigma_{22}, \ell_2, 5/3, 1/3; k\right), \qquad (63)$$

and

$$F_V\left(k\right) = \frac{1}{2} F_0\left(\sigma_{33}, \ell_3, 5/3, 1/3; k\right). \qquad (64)$$

The 1D spectra for the bottom-up von Kármán model are plotted in figures 3 to 5. Agreement with the Kaimal *et al* equations is fair. The main difference for all three cases is that the von Kármán model curves are more sharply peaked than the Kaimal *et al* equations and have less energy at small kz.

5.2   Anisotropic Energy Spectra

To derive the anisotropic energy spectra, we follow the method developed by Kristensen *et al* (1989). Their equations (49) to (50) for the $A_i\left(k\right)$ can be written in the following form:

$$A_1\left(k\right) = \frac{k}{4\pi} \frac{d}{dk} \frac{1}{k} \frac{dF_L\left(k\right)}{dk} + \frac{1}{2\pi} \left[-\beta\left(k^{-2}\right) - \zeta\left(k^{-2}\right)\right], \qquad (65)$$

$$A_2\left(k\right) = \frac{k}{4\pi} \frac{d}{dk} \frac{1}{k} \frac{dF_L\left(k\right)}{dk} + \frac{1}{2\pi} \left[\alpha\left(k^{-2}\right) - 3\beta\left(k^{-2}\right) - \zeta\left(k^{-2}\right)\right], \qquad (66)$$

and

$$A_3\left(k\right) = \frac{k}{4\pi} \frac{d}{dk} \frac{1}{k} \frac{dF_L\left(k\right)}{dk} + \frac{1}{2\pi} \left[-\alpha\left(k^{-2}\right) - 3\beta\left(k^{-2}\right) - \zeta\left(k^{-2}\right)\right]. \qquad (67)$$

The first term in equations (65) to (67) represents the isotropic contribution. By differentiation of equation (62), this term is found to be

$$\frac{k}{4\pi} \frac{d}{dk} \frac{1}{k} \frac{dF_L\left(k\right)}{dk} = \frac{55 \sigma_{11}^2}{36\pi B\left(1/2, 1/3\right)} \frac{k^2 \ell_1^5}{\left(1 + k^2 \ell_1^2\right)^{17/6}}. \qquad (68)$$

Derivation of the terms in equations (65) to (67) that involve the functions $\alpha\left(s\right)$, $\beta\left(s\right)$, and $\zeta\left(s\right)$ begins by defining the "residual" functions

$$H\left(k\right) = F_T\left(k\right) - F_V\left(k\right), \qquad (69)$$

and

$$J(k) = F_L(k) - kF'_L(k) - [F_T(k) + F_V(k)].$$ (70)

In isotropic turbulence, the residual functions are zero. It is convenient also to define

$$f(s) = H\left(s^{-1/2}\right)s^2,$$ (71)

and

$$g(s) = J\left(s^{-1/2}\right)s^2,$$ (72)

where

$$s \equiv k^{-2}.$$ (73)

From equations (62) to (64), we find

$$f(s) = \frac{s^2}{2}\left[F_0\left(\sigma_{22}, \ell_2, 5/3, 1/3; s^{-1/2}\right) - F_0\left(\sigma_{33}, \ell_3, 5/3, 1/3; s^{-1/2}\right)\right],$$ (74)

and

$$g(s) = \frac{s^2}{2}\left[2F_0\left(\sigma_{11}, \ell_1, 5/3, 1/3; s^{-1/2}\right) - F_0\left(\sigma_{22}, \ell_2, 5/3, 1/3; s^{-1/2}\right)\right.$$
$$\left. - F_0\left(\sigma_{33}, \ell_3, 5/3, 1/3; s^{-1/2}\right)\right].$$ (75)

The functions $\alpha(s)$, $\beta(s)$, and $\zeta(s)$ in equations (65) to (67) can be determined from the integrals (Kristensen *et al*, 1989)

$$\alpha(s) = \frac{s^{+1/\sqrt{2}}}{\sqrt{2}}\int_0^s t^{1-1/\sqrt{2}}f'''(t)\,dt - \frac{s^{-1/\sqrt{2}}}{\sqrt{2}}\int_0^s t^{1+1/\sqrt{2}}f'''(t)\,dt,$$ (76)

$$\beta(s) = \frac{s^{1/3}}{3}\int_0^s t^{2/3}g'''(t)\,dt, \quad \text{and}$$ (77)

$$\zeta(s) = -s^{-1}\int_0^s t^2g'''(t)\,dt.$$ (78)

Hence we need to solve integrals of the form

$$I(\sigma, \ell, q; s) = \frac{qs^q}{2}\int_0^s t^{1-q}\frac{d^3}{dt^3}\left[t^2F_0\left(\sigma, \ell, 5/3, 1/3; t^{-1/2}\right)\right]\,dt,$$ (79)

and we have

25

$$\alpha\left(s\right) = I\left(\sigma_{22}, \ell_2, \frac{1}{\sqrt{2}}; s\right) - I\left(\sigma_{33}, \ell_3, \frac{1}{\sqrt{2}}; s\right) + I\left(\sigma_{22}, \ell_2, -\frac{1}{\sqrt{2}}; s\right)$$

$$- I\left(\sigma_{33}, \ell_3, -\frac{1}{\sqrt{2}}; s\right), \tag{80}$$

$$\beta\left(s\right) = 2I\left(\sigma_{11}, \ell_1, \frac{1}{3}; s\right) - I\left(\sigma_{22}, \ell_2, \frac{1}{3}; s\right) - I\left(\sigma_{33}, \ell_3, \frac{1}{3}; s\right), \tag{81}$$

and

$$\zeta\left(s\right) = 2I\left(\sigma_{11}, \ell_1, -1; s\right) - I\left(\sigma_{22}, \ell_2, -1; s\right) - I\left(\sigma_{33}, \ell_3, -1; s\right). \tag{82}$$

It can be shown that

$$\frac{d}{dt}F_0\left(\sigma, \ell, a, \nu; t^{-1/2}\right) = \frac{\nu\left(\nu - a + 1/2\right)}{\nu + 1/2}\frac{\ell^2}{s^2}F_0\left(\sigma, \ell, \frac{a\left(\nu + 3/2\right)}{\nu - a + 1/2}, \nu + 1; t^{-1/2}\right),$$

from which follows

$$\frac{d^3}{dt^3}\left[t^2 F_0\left(\sigma, \ell, a, \nu; t^{-1/2}\right)\right] = c_3\frac{\ell^6}{s^4}F_0\left(\sigma, \ell, a_3, \nu_3; t^{-1/2}\right),$$

where

$$c_{n+1} = \frac{\nu_n\left(\nu_n - a_n + 1/2\right)}{\nu_n + 1/2}c_n, \quad a_{n+1} = \frac{a_n\left(\nu_n + 3/2\right)}{\nu_n - a_n + 1/2}, \quad \nu_{n+1} = \nu_n + 1,$$

and

$$c_0 = 1, \quad a_0 = a = \frac{5}{3}, \quad \nu_0 = \nu = \frac{1}{3}.$$

(The c_i's defined in this section are different from those in sect. 3 .) It can be shown that

$$c_3 = -\frac{140}{27}, \quad a_3 = -\frac{23}{15}, \quad \nu_3 = \frac{10}{3}.$$

Hence

$$\frac{d^3}{dt^3}\left[t^2 F_0\left(\sigma, \ell, 5/3, 1/3; t^{-1/2}\right)\right] = -\frac{140}{27}\frac{\ell^6}{s^4}F_0\left(\sigma, \ell, -\frac{23}{15}, \frac{10}{3}; t^{-1/2}\right)$$

$$= -\frac{4675}{216}\frac{\sigma^2}{\ell B\left(1/2, 1/3\right)}\frac{\left(t/\ell^2\right)^{-1/6}}{\left(1 + t/\ell^2\right)^{23/6}}\left(1 - \frac{23}{15}\frac{1}{1 + t/\ell^2}\right).$$

26

With the help of equation (A-7), we now find

$$
\begin{aligned}
I\left(\sigma, \ell, q; s\right) = \ & \frac{4675}{432} \frac{q\sigma^2 \ell^3}{B\left(1/2, 1/3\right)} \left(\frac{s}{\ell^2}\right)^q \left[\frac{23}{15} B_{s/\ell^2/(1+s/\ell^2)}\left(\frac{11}{6} - q, 3 + q\right)\right. \\
& \left. - B_{s/\ell^2/(1+s/\ell^2)}\left(\frac{11}{6} - q, 2 + q\right)\right],
\end{aligned}
\tag{83}
$$

where

$$
B_z\left(a, b\right) = \int_0^z s^{a-1}\left(1 - s\right)^{b-1} ds
\tag{84}
$$

is the incomplete beta function. Substitution of this result into equations (80) to (82) yields the functions $\alpha\left(s\right)$, $\beta\left(s\right)$, and $\zeta\left(s\right)$, and hence the anisotropic energy spectra.

The anisotropic energy spectra for the bottom-up von Kármán model are shown in figures 6 to 8. One notable feature of the A_3-curve is that it is initially negative and then becomes positive for $kz > 2$. This behavior is somewhat alarming, since an energy spectrum must strictly be non-negative. The behavior could result from vertical inhomogeneities characteristic of a shear layer, which are neglected in the present model.

5.3 2D Correlation Functions

The 2D correlation function $b_{11,1}\left(r_\perp\right)$ can be found by substituting equation (65) into equation (46). The isotropic contribution, given by equation (68), is therefore

$$
\int_0^\infty \left[\frac{k^2}{2} \frac{d}{dk} \frac{1}{k} \frac{dF_L\left(k\right)}{dk}\right] J_0\left(kr\right) dk = \frac{55\sigma_{11}^2}{18B\left(1/2, 1/3\right)} \int_0^\infty \left[\frac{k^3 \ell_1^5}{\left(1 + k^2 \ell_1^2\right)^{17/6}}\right] J_0\left(kr\right) dk.
\tag{85}
$$

The recurrence relation for Bessel functions allows us to write $J_0\left(kr\right) = (2/kr)J_1\left(kr\right) - J_2\left(kr\right)$. This leaves two integrals, each of which can be solved using equation (6.565.4) in Gradshteyn and Ryzhik (1994). The result is

$$
\int_0^\infty \left[\frac{k^2}{2} \frac{d}{dk} \frac{1}{k} \frac{dF_L\left(k\right)}{dk}\right] J_0\left(kr\right) dk = \frac{2\sigma_{11}^2 \ell_1}{\sqrt{\pi}\Gamma\left(1/3\right)} \left(\frac{r}{2\ell_1}\right)^{5/6} \left[K_{5/6}\left(\frac{r}{\ell_1}\right) - \frac{r}{2\ell_1} K_{1/6}\left(\frac{r}{\ell_1}\right)\right].
\tag{86}
$$

Calculation of the anisotropic contribution to $b_{11,1}\left(r\right)$ is rather difficult. We need to solve integrals of the form

$$
\overline{I}\left(\sigma, \ell, q; r\right) = \int_0^\infty I\left(\sigma, \ell, q; k^{-2}\right) J_0\left(kr\right) k \, dk,
\tag{87}
$$

in which $I\left(\sigma, \ell, q ; k^{-2}\right)$ contains incomplete beta functions (eq (83)). One possible approach, based on rewriting the incomplete beta function as a Meijer's G-function, is discussed in the appendix. Using equation (A-12), we find

$$
\begin{aligned}
\overline{I}\left(\sigma, \ell, q ; r\right) = & \frac{q\sigma^2\ell}{2\sqrt{\pi}\Gamma\left(1/3\right)}\left(\frac{r}{2\ell}\right)^{11/3}\left[G_{42}^{22}\left(\frac{4\ell^2}{r^2}\middle|\begin{array}{l}17/6, \ 2, \ 23/6-q, \ 17/6\\17/6-q, \ 35/6\end{array}\right)\right.\\
& \left. -\frac{5}{2}\ G_{42}^{22}\left(\frac{4\ell^2}{r^2}\middle|\begin{array}{l}17/6, \ 2, \ 23/6-q, \ 17/6\\17/6-q, \ 29/6\end{array}\right)\right].
\end{aligned}
\tag{88}
$$

For the 2D correlation function in the along-wind direction, we now have from equation (65)

$$
b_{11,1}\left(r\right) = \frac{2\sigma_{11}^2\ell_1}{\sqrt{\pi}\Gamma\left(1/3\right)}\left(\frac{r}{2\ell_1}\right)^{5/6}\left[K_{5/6}\left(\frac{r}{\ell_1}\right)-\frac{r}{2\ell_1}K_{1/6}\left(\frac{r}{\ell_1}\right)\right]-\overline{\beta}\left(r\right)-\overline{\zeta}\left(r\right),
\tag{89}
$$

where, from eq (27),

$$
\overline{\beta}\left(r\right) = 2\overline{I}\left(\sigma_{11}, \ell_1, \frac{1}{3}; r\right) - \overline{I}\left(\sigma_{22}, \ell_2, \frac{1}{3}; r\right) - \overline{I}\left(\sigma_{33}, \ell_3, \frac{1}{3}; r\right).
\tag{90}
$$

Equations for $b_{22,2}\left(r\right)$, $b_{33,3}\left(r\right)$, $\overline{\alpha}\left(r\right)$, and $\overline{\zeta}\left(r\right)$ follow with obvious replacements.

Since routines for computing Meijer's G-functions are not widely available,[*] calculating the 2D correlations using equation (88) is not normally practical. Rather, they must be calculated by performing the integration in equation (87) numerically. Generalization of the isotropic von Kármán model to the anisotropic case, using a bottom-up approach, therefore prevents us from obtaining important results such as the 2D correlations in a convenient analytical form—a rather disappointing outcome.

Computations of the 2D structure functions, found by numerical integration, are shown in figures 9 to 10. The results are observed to differ significantly from the top-down approach.

5.4 Parameter Selection

As was the case for the top-down approach, I choose the variances for the bottom-up anisotropic von Kármán model to match Kaimal *et al*'s results, shown in table 1. The length scale parameters are chosen to produce the

---

[*]H. Auvermann has shown that the commercial software package Mathematica contains a routine to compute Meijer's G-functions.

correct inertial-subrange asymptote, just as in section 4.5. From equations (53) and (108), we have for $k\ell_1 \gg 1$,

$$F_L(k) \cong \frac{1}{B(1/2, 1/3)} \sigma_{11}^2 \ell_1^{-2/3} k^{-5/3} = \frac{\alpha}{2} \epsilon^{2/3} k^{-5/3}.$$

Solving for ℓ_1, we find

$$\ell_1 = \left[\frac{2\sigma_{11}^2}{\alpha B(1/2, 1/3)} \right]^{3/2} \frac{\kappa z}{u_*^3} \simeq 0.350 \frac{\sigma_{11}^3 z}{u_*^3} \simeq 3.64z. \tag{91}$$

It follows from equation (58) that

$$F_T(k) = F_V(k) = \frac{4}{3} F_L(k) \tag{92}$$

in the inertial subrange. Hence for $k\ell_2 \gg 1$,

$$F_T(k) \cong \frac{4}{3B(1/2, 1/3)} \sigma_{11}^2 \ell_1^{-2/3} k^{-5/3} = \frac{2\alpha}{3} \epsilon^{2/3} k^{-5/3},$$

and

$$\ell_2 = \left[\frac{2\sigma_{22}^2}{\alpha B(1/2, 1/3)} \right]^{3/2} \frac{\kappa z}{u_*^3} \simeq 0.350 \frac{\sigma_{22}^3 z}{u_*^3} \simeq 1.53z. \tag{93}$$

Similarly,

$$\ell_3 = \left[\frac{2\sigma_{33}^2}{\alpha B(1/2, 1/3)} \right]^{3/2} \frac{\kappa z}{u_*^3} \simeq 0.350 \frac{\sigma_{33}^3 z}{u_*^3} \simeq 0.617z. \tag{94}$$

6. Kristensen *et al* Model

Krasnenko *et al* (1997) have previously suggested using the Kristensen *et al* (1989) model to calculate statistics of acoustic field fluctuations. This model is very similar to the bottom-up von Kármán model discussed in the previous section. In fact, I based the derivation in the previous section largely on Kristensen *et al*'s model. The main comparative advantage of the Kristensen *et al* model is its flexibility. It contains additional parameters that allow one to tailor the shape of the spectral "peak" to the data set. The disadvantages are that the equations are somewhat more complicated and that, in some cases, deriving values for all of the parameters may be difficult. The equations for the Kristensen *et al* model are summarized below in a slightly different form than in the original paper. The changes hopefully make computations somewhat simpler.

6.1 1D Spectral Densities

Kristensen *et al* used the following equations for the 1D spectra for wave numbers corresponding to the direction of the mean wind:

$$F_L(k) = \Theta_{11,1}(k) = \frac{L_{11,1}\sigma_{11}^2}{\pi} \frac{1}{\left\{ 1 + \left[\frac{kL_{11,1}}{a(\mu_1)} \right]^{2\mu_1} \right\}^{5/6\mu_1}}, \tag{95}$$

$$F_T(k) = \Theta_{22,1}(k) = \frac{L_{22,1}\sigma_{22}^2}{2\pi} \frac{1 + \frac{8}{3}\left[\frac{kL_{22,1}}{a(\mu_2)} \right]^{2\mu_2}}{\left\{ 1 + \left[\frac{kL_{22,1}}{a(\mu_2)} \right]^{2\mu_2} \right\}^{5/6\mu_2 + 1}}, \tag{96}$$

and

$$F_V(k) = \Theta_{33,1}(k) = \frac{L_{33,1}\sigma_{33}^2}{2\pi} \frac{1 + \frac{8}{3}\left[\frac{kL_{33,1}}{a(\mu_3)} \right]^{2\mu_3}}{\left\{ 1 + \left[\frac{kL_{33,1}}{a(\mu_3)} \right]^{2\mu_3} \right\}^{5/6\mu_3 + 1}}, \tag{97}$$

where

$$a(\mu) = \frac{\pi\mu}{B(1/2\mu, 1/3\mu)}. \tag{98}$$

The parameters μ_i control the sharpness of the spectral peak; larger values give a sharper peak. A value of 1 corresponds to the bottom-up anisotropic von Kármán model.

The 1D spectra for the Kristensen *et al* model are plotted in figures 3 to 5 and compared to Kaimal *et al* equations, as well as the two versions of the von Kármán model. (Selection of the parameters for this model will be discussed in sect. 6.4.) It is seen that the Kristensen *et al* model has enough flexibility in its equations to reproduce Kaimal *et al*'s empirical equations quite well.

6.2 Anisotropic Energy Spectra

Derivation of the anisotropic energy spectra $A_i(k)$ proceeds much as it did in section 5, except that the equations become somewhat more complicated because of the more complicated form for the 1D spectra. The first term in equations (65) to (67), representing the isotropic spectra, is found by differentiation of equation (96) to be

$$\frac{k}{4\pi}\frac{d}{dk}\frac{1}{k}\frac{dF_L(k)}{dk} = \frac{5\sigma_{11}^2}{12\pi^2 a^{2\mu_1}(\mu_1)}\frac{k^{2\mu_1-2}L_{11,1}^{2\mu_2+1}}{\left\{1+\left[\frac{kL_{11,1}}{a(\mu_1)}\right]^{2\mu_1}\right\}^{5/6\mu_1+2}}\left\{2-2\mu_1+\frac{11}{3}\left[\frac{kL_{11,1}}{a(\mu_1)}\right]^{2\mu_1}\right\}. \quad (99)$$

The remaining terms in equations (65) to (67), involving the functions $\alpha(s)$, $\beta(s)$, and $\zeta(s)$, represent the anisotropic contributions. Since the reader can refer to the solution for these functions in Kristensen *et al* (1989), it will not be repeated here. The functions are given by the equations

$$\begin{aligned}\alpha(s) =\ & \gamma_0\left(\frac{1}{\sqrt{2}},\sigma_{22},L_{22,1},\mu_2;s\right)-\gamma_0\left(\frac{1}{\sqrt{2}},\sigma_{33},L_{33,1},\mu_3;s\right)\\ & +\gamma_0\left(-\frac{1}{\sqrt{2}},\sigma_{22},L_{22,1},\mu_2;s\right)-\gamma_0\left(-\frac{1}{\sqrt{2}},\sigma_{33},L_{33,1},\mu_3;s\right),\end{aligned} \quad (100)$$

$$\beta(s) = 2\gamma_0\left(\frac{1}{3},\sigma_{11},L_{11,1},\mu_1;s\right)-\gamma_0\left(\frac{1}{3},\sigma_{22},L_{22,1},\mu_2;s\right)-\gamma_0\left(\frac{1}{3},\sigma_{33},L_{33,1},\mu_3;s\right), \quad (101)$$

and

$$\zeta(s) = 2\gamma_0\left(-1,\sigma_{11},L_{11,1},\mu_1;s\right)-\gamma_0\left(-1,\sigma_{22},L_{22,1},\mu_2;s\right)-\gamma_0\left(-1,\sigma_{33},L_{33,1},\mu_3;s\right). \quad (102)$$

The function γ_0 is in turn given by

$$\gamma_0(q,\sigma,\ell,\mu;s) = \frac{1}{96\pi}\frac{q\sigma^2\ell^3}{\mu a^2(\mu)}\eta^q\sum_{n=1}^{4}C_n(\mu)\,B_{\eta^\mu/(1+\eta^\mu)}\left(\frac{11}{6\mu}-\frac{q}{\mu},n+\frac{q-1}{\mu}\right), \quad (103)$$

where

$$\eta \equiv \frac{a^2(\mu)}{\ell^2} s, \tag{104}$$

and

$$\left. \begin{array}{l} C_1(\mu) = 40\,(1-\mu)\,(1-2\mu)\,(2-\mu) \\ C_2(\mu) = \frac{140}{3}\,(1-\mu)\,(1-2\mu)\,(5+6\mu) \\ C_3(\mu) = \frac{10}{9}\,(5+6\mu)\,(5+12\mu)\,(7-12\mu) \\ C_4(\mu) = \frac{10}{27}\,(5+6\mu)\,(5+12\mu)\,(5+18\mu) \end{array} \right\}. \tag{105}$$

The anisotropic energy spectra for the Kristensen *et al* model are plotted in figures 6 to 8 and compared to the models discussed in previous sections. The curves for the Kristensen *et al* model are similar to the bottom-up von Kármán model, although they appear more flattened. As was the case for the bottom-up von Kármán model, the Kristensen *et al* model exhibits negative A_3 for small kz. Since the Kristensen *et al* model fits Kaimal *et al*'s 1D spectra so well, the cause of this feature must either be that the 1D spectral measurements are inaccurate or that the turbulence cannot be adequately modeled using equation (23).

6.3 2D Correlation Functions

In order to find the 2D correlations, we need to solve the integral equation (46), with A_1 given by equation (65). For the Kristensen *et al* model, we must calculate integrals of the form

$$\int_0^\infty \gamma_0\left(q, \sigma, L, \mu; k^{-2}\right) J_0(kr)\, k\, dk.$$

I have been unable to find a method for calculating these integrals. Apparently one cannot even express the result in terms of Meijer's G-functions, as was possible for the bottom-up von Kármán model. Fortunately, finding the 2D correlations by performing a numerical integration is not difficult.

Predictions from the Kristensen *et al* model are compared to the von Kármán family in figures 9 to 10. Comparisons to the anisotropic Gaussian and Mann models (to be discussed later in this report) are shown in figures 11 to 12. The Kristensen *et al* model predicts a strong enhancement of the 2D structure function in the along-wind direction, and a slight enhancement in the crosswind direction.
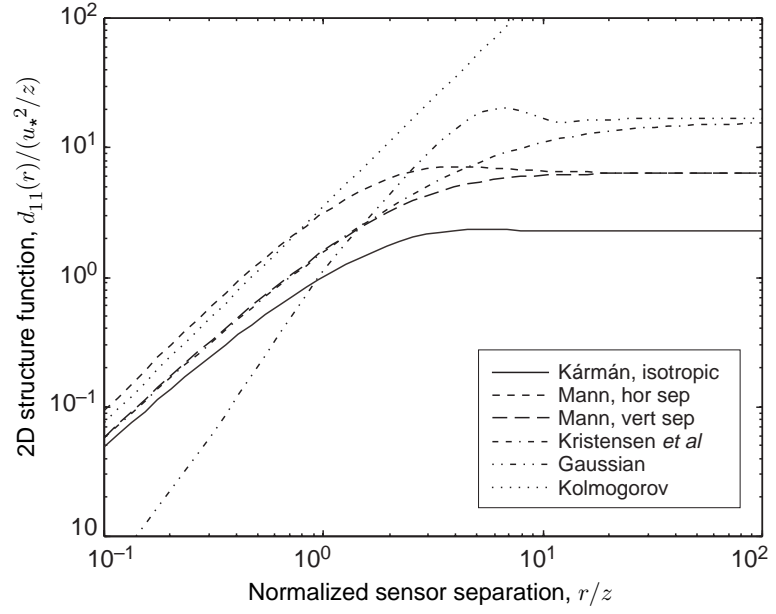
Figure 11. Predictions of 2D structure function for along-wind direction for Kristensen *et al*, Gaussian, isotropic von Kármán, Kolmogorov, and Mann models.
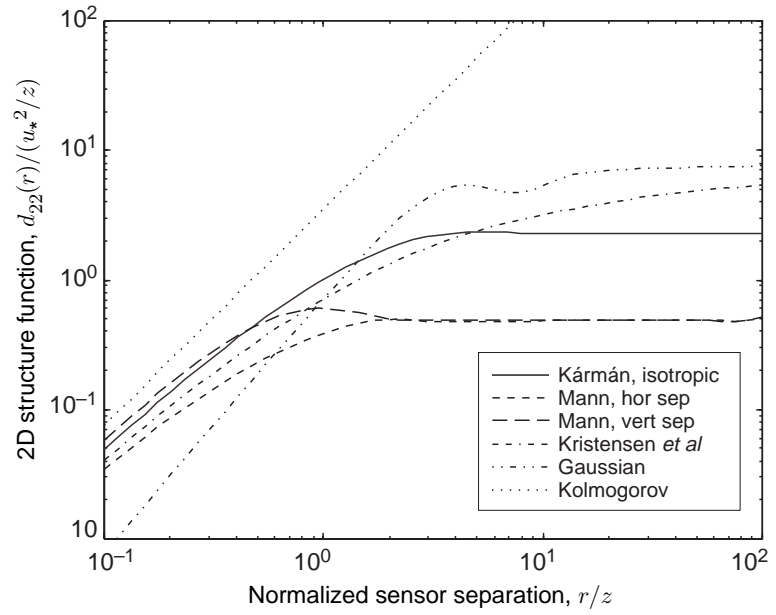
Figure 12. Predictions of 2D structure function for crosswind direction, for Kristensen *et al*, Gaussian, isotropic von Kármán, Kolmogorov, and Mann models.

6.4 Parameter Selection

Kristensen *et al* chose the variances and integral length scales in their model to match those found by Kaimal *et al*, and hence the values for these parameters are the same as in table 1. They also determined the parameters μ_i by fitting their model to Kaimal *et al*'s equations. The result is

$$\left.\begin{array}{l} \mu_1 = 0.52 \\ \mu_2 = 0.49 \\ \mu_3 = 0.68 \end{array}\right\} . \tag{106}$$

Note that the μ_i's deviate significantly from 1, indicating that the actual spectra are less peaked than in the von Kármán model.

7. Gaussian Model

Although it is rather unrealistic, the isotropic Gaussian model has proven quite popular. The main advantage of the isotropic Gaussian model is that the equations for the correlation and spectral functions are easily obtainable. In this section, we explore how the Gaussian model can be generalized to the anisotropic case using a bottom-up approach. Since convenient closed-form results could not be obtained for quantities such as the 2D correlations in the bottom-up von Kármán model, it is interesting to see whether such results can be obtained for the Gaussian model.

7.1 1D Spectral Densities

For this model it is assumed that the longitudinal correlation function has the form

$$R_{11}\left(r\hat{\mathbf{e}}_1\right) = \sigma_{11}^2 \exp\left(-\frac{r^2}{\ell_1^2}\right). \tag{107}$$

By calculating the Fourier transform according to equation (10) we find

$$F_L\left(k\right) = \Theta_{11,1}\left(k\right) = \frac{\sigma_{11}^2 \ell_1}{2\sqrt{\pi}} \exp\left(-\frac{k^2\ell_1^2}{4}\right). \tag{108}$$

As mentioned before, $F_T\left(k\right) = F_V\left(k\right) = (1/2)\left[F_L\left(k\right) - kF_L'\left(k\right)\right]$ in isotropic turbulence. Since

$$F_L\left(k\right) - kF_L'\left(k\right) = \frac{\sigma_{11}^2 \ell_1}{2\sqrt{\pi}}\left(1 + \frac{k^2\ell_1^2}{2}\right)\exp\left(-\frac{k^2\ell_1^2}{4}\right), \tag{109}$$

natural choices for $F_T\left(k\right)$ and $F_V\left(k\right)$ are

$$F_T\left(k\right) = \Theta_{22,1}\left(k\right) = \frac{\sigma_{22}^2 \ell_2}{4\sqrt{\pi}}\left(1 + \frac{k^2\ell_2^2}{2}\right)\exp\left(-\frac{k^2\ell_2^2}{4}\right), \text{ and} \tag{110}$$

$$F_V\left(k\right) = \Theta_{33,1}\left(k\right) = \frac{\sigma_{33}^2 \ell_3}{4\sqrt{\pi}}\left(1 + \frac{k^2\ell_3^2}{2}\right)\exp\left(-\frac{k^2\ell_3^2}{4}\right). \tag{111}$$

The 1D spectra for the anisotropic Gaussian model are plotted in figures 3 to 5, which also show the models discussed in previous sections of this report. (Selection of the parameters for the Gaussian model will be described in sect. 7.4.) The Gaussian model is observed to agree with Kaimal *et al*'s equations for very small kz. However, the spectral peak in the Gaussian model is much too sharp, and the inertial-subrange decay is much too rapid.

7.2 Anisotropic Energy Spectra

We will again determine the anisotropic energy spectra using equations (65) to (67). The isotropic term in those equations is, for the Gaussian model,

$$\frac{k}{4\pi}\frac{d}{dk}\frac{1}{k}\frac{dF_L(k)}{dk} = \frac{\sigma_{11}^2 k^2 \ell_1^5}{32\pi^{3/2}}\exp\left(-\frac{k^2\ell_1^2}{4}\right).\tag{112}$$

Using the same method as in section 5.2 to calculate $\alpha(s)$, $\beta(s)$, and $\zeta(s)$, we arrive at the residual functions

$$f(s) = \frac{s^2}{2}\left[F_0\left(\sigma_{22}, \ell_2; s^{-1/2}\right) - F_0\left(\sigma_{33}, \ell_3; s^{-1/2}\right)\right], \text{ and}$$

$$g(s) = \frac{s^2}{2}\left[2F_0\left(\sigma_{11}, \ell_1; s^{-1/2}\right) - F_0\left(\sigma_{22}, \ell_2; s^{-1/2}\right) - F_0\left(\sigma_{33}, \ell_3; s^{-1/2}\right)\right],$$

where

$$F_0(\sigma, \ell; k) = \frac{\sigma^2 \ell}{2\sqrt{\pi}}\left(1 + \frac{k^2\ell^2}{2}\right)\exp\left(-\frac{k^2\ell^2}{4}\right).\tag{113}$$

We again need to find integrals of the form given by equation (79), although with the function F_0 given by equation (111), we can show that

$$\frac{d^3}{dt^3}\left[t^2 F_0\left(\sigma, \ell; t^{-1/2}\right)\right] = \frac{\sigma^2 \ell}{2\sqrt{\pi}}\left[\left(-\frac{5\ell^6}{64t^4} + \frac{\ell^8}{128t^5}\right)\exp\left(-\frac{\ell^2}{4t}\right)\right].$$

The integrals can now be found using equation (A-9), with result

$$I(\sigma, \ell, q; s) = \frac{q\sigma^2 \ell^3}{8\sqrt{\pi}}\left(\frac{4s}{\ell^2}\right)^q\left[\Gamma\left(3+q, \frac{\ell^2}{4s}\right) - \frac{5}{2}\Gamma\left(2+q, \frac{\ell^2}{4s}\right)\right].\tag{114}$$

The functions $\alpha(s)$, $\beta(s)$, and $\zeta(s)$ can now be determined using equations (80) to (82).

The anisotropic energy spectra for the Gaussian model are plotted in figures 6 to 8. They have a rather strange and unphysical appearance, exhibiting multiple positive and negative peaks as kz is varied.

7.3 2D Correlation Functions

It is not difficult to calculate the isotropic contribution to the 2D correlation functions in the Gaussian model. Substituting equation (112) into (46), we have the following integral for the isotropic contribution:

$$\int_0^\infty \left[\frac{k^2}{2}\frac{d}{dk}\frac{1}{k}\frac{dF_L(k)}{dk}\right] J_0(kr)\, dk = \frac{\sigma_{11}^2 \ell_1^5}{16\sqrt{\pi}}\int_0^\infty \exp\left(-\frac{k^2\ell_1^2}{4}\right) J_0(kr)\, k^3\, dk.\tag{115}$$

Using the recurrence relation for Bessel functions, we have two integrals, each of which can be solved using Gradshteyn and Ryzhik's (1994) equation (6.63.4). The result is

$$\int_0^\infty \left[\frac{k^2}{2} \frac{d}{dk} \frac{1}{k} \frac{dF_L(k)}{dk} \right] J_0(kr)\, dk = \frac{\sigma_{11}^2 \ell_1}{2\sqrt{\pi}} \left(1 - \frac{r^2}{\ell_1^2} \right) \exp \left(-\frac{r^2}{\ell_1^2} \right). \quad (116)$$

The calculations for the anisotropic contributions are more complicated, requiring us to integrate incomplete gamma functions. Specifically, we must calculate integrals of the form

$$\overline{I}(\sigma, \ell, q; r) = \int_0^\infty I\left(\sigma, \ell, q; k^{-2}\right) J_0(kr)\, k\, dk = \frac{q\sigma^2 \ell^3}{8\sqrt{\pi}} \int_0^\infty \left(\frac{4}{k^2 \ell^2} \right)^q$$
$$\left[\Gamma \left(3 + q, \frac{k^2 \ell^2}{4} \right) - \frac{5}{2} \Gamma \left(2 + q, \frac{k^2 \ell^2}{4} \right) \right] J_0(kr)\, k\, dk. \quad (117)$$

To solve an integral of this form, I will rewrite the incomplete gamma functions in terms of confluent hypergeometric functions. From equations (13.1.33) and (13.6.28) in Abramowitz and Stegun (1965), we have

$$\Gamma(a, x) = e^{-x/2} x^{a/2 - 1/2} W_{a/2 - 1/2, -a/2}(x), \quad (118)$$

where $W_{\kappa, \mu}(\cdot)$ is Whittaker's function. Hence

$$I(\sigma, \ell, q; s) = \frac{q\sigma^2 \ell^3}{8\sqrt{\pi}} \left(\frac{4s}{\ell^2} \right)^{q/2} \exp \left(-\frac{\ell^2}{8s} \right)$$
$$\times \left[\left(-\frac{\ell^2}{4s} \right) W_{1+q/2, 3/2+q/2} \left(\frac{\ell^2}{4s} \right) - \frac{5}{2} \left(-\frac{\ell^2}{4s} \right)^{1/2} W_{1/2+q/2, 1+q/2} \left(\frac{\ell^2}{4s} \right) \right]. \quad (119)$$

The integration can now be performed using Gradshteyn and Ryzhik's (1994) equation (7.672.2), with result

$$\overline{I}(\sigma, \ell, q; r) = \frac{3q\sigma^2 \ell}{2\sqrt{\pi}(1-q)} \left[{}_2F_2 \left(4, 1-q; 1, 2-q; -\frac{r^2}{\ell^2} \right) \right.$$
$$\left. - \frac{5}{4} {}_2F_2 \left(3, 1-q; 1, 2-q; -\frac{r^2}{\ell^2} \right) \right], \quad (120)$$

where ${}_2F_2(\cdot)$ is a generalized hypergeometric function.

Although we have managed to integrate the anisotropic part, the result is not very helpful from a practical standpoint. Routines are not commonly

available to calculate generalized hypergeometric functions. Hence the 2D correlations must be calculated numerically, by integrating equation (46). This is a rather surprising outcome: even the simple Gaussian model, when generalized to the anisotropic case, eludes a convenient solution for the 2D correlation function.

Predictions of the 2D structure function from the anisotropic Gaussian model (calculated by numerical integration) are compared to the Kristensen *et al* model in figures 11 to 12. The Gaussian model converges on the Kristensen *et al* model for sensor separations much larger than the height, since the two models are essentially the same at large scales of the energy subrange. However, at smaller separations, corresponding to the inertial subrange, the Gaussian model predictions are quite unrealistic. Furthermore, the Gaussian model exhibits unphysical peaks in the 2D structure function around the transition between the inertial and energy subranges.

7.4   Parameter Selection

Since the Gaussian model does not have a realistic inertial subrange, it is logical to select its parameters to obtain the best possible fit to spectral characteristics of the energy subrange, such as variances and integral length scales. Hence I take the approach here of selecting the Gaussian model parameters to reproduce the variances and integral length scales given in table 1. To reproduce the variances, of course, we simply assign the variances in the Gaussian model to those given in the table. The length scales follow from equation (18). Evaluating equations (108), (111), and (111) at $k = 0$, we find

$$L_{11,1} = \frac{\sqrt{\pi}}{2}\ell_1, \ L_{22,1} = \frac{\sqrt{\pi}}{4}\ell_2, \ L_{33,1} = \frac{\sqrt{\pi}}{4}\ell_3.$$

The resulting Gaussian model parameters are shown in table 3.

Table 3. Values for variances σ_{ii}^2 and length scales ℓ_i corresponding to Gaussian model.

i	σ_{ii}^2	ℓ_i
1	$4.77u_*^2$	$6.21z$
2	$2.68u_*^2$	$3.59z$
3	$1.46u_*^2$	$0.774z$

8. Mann Model

8.1 Rapid Distortion Theory and Eddy Lifetimes

The Mann model is the result of a "first-principle" theoretical treatment for turbulence in a constant shear layer. By *constant shear*, it is meant that the gradient, dU/dz (where U is the mean wind speed), is constant. Constant dU/dz implies, of course, that U is proportional to z. In an actual shear layer, U is proportional to the logarithm of z. Except for this shortcoming, the Mann model is probably quite realistic.

The main hypothesis upon which Mann's model is based is called *rapid distortion theory*. The idea is basically this: In a turbulent shear layer, new eddies are perpetually being created, subjected to the forces of shear, and then eventually broken down. Between the times when an eddy is "created" and when it is "destroyed" by the shear, there is a time at which the eddy exists in a state that is "typical" for eddies having its same spatial dimensions. Let us call this "typical" time the *eddy lifetime*. This argument suggests that we can derive a spectral model by introducing turbulence with some energy spectrum $E(k)$ at time $t = 0$ and then subjecting the turbulence to shear (i.e., rapidly distorting it) for a time interval equal to the eddy lifetime. Then the spectrum should be roughly the same as turbulence in the actual shear layer.

The initial energy spectrum $E(k)$ in Mann's model is the von Kármán energy spectrum, equation (1). The eddy lifetime being given in nondimensional form (depends) on the scale of the eddies by[*]

$$\beta = \Gamma \left(k\ell\right)^{-2/3} \left\{ {}_2F_1 \left[\frac{1}{3}, \frac{17}{6}; \frac{4}{3}; -\left(k\ell\right)^{-2} \right] \right\}^{-1/2}, \qquad (121)$$

in which Γ is a model parameter. Values for Γ in the range of 2.6 to 3.8 appear to be reasonable for atmospheric turbulence (Mann, 1994).

A full discussion of rapid distortion theory and Mann's model is beyond the scope of this report. The results of the analysis, as they pertain to acoustical propagation modeling, will be summarized in the following sections.

---

[*]The nondimensional eddy lifetime is dimensionalized by multiplication by $(dU/dz)^{-1}$.

8.2 3D Spectral Densities

Mann's equations for the spectra in a uniform (constant gradient) shear layer are

$$\Phi_{11}(\mathbf{k}) = \frac{E(k_0)}{4\pi k_0^4}\left[k_0^2 - k_1^2 - 2k_1 k_{30}\zeta_1 + \left(k_1^2 + k_2^2\right)\zeta_1^2\right], \tag{122}$$

$$\Phi_{22}(\mathbf{k}) = \frac{E(k_0)}{4\pi k_0^4}\left[k_0^2 - k_2^2 - 2k_2 k_{30}\zeta_2 + \left(k_1^2 + k_2^2\right)\zeta_2^2\right], \tag{123}$$

$$\Phi_{12}(\mathbf{k}) = \frac{E(k_0)}{4\pi k_0^4}\left[-k_1 k_2 - k_1 k_{30}\zeta_2 - k_2 k_{30}\zeta_1 + \left(k_1^2 + k_2^2\right)\zeta_1\zeta_2\right], \tag{124}$$

$$\Phi_{13}(\mathbf{k}) = \frac{E(k_0)}{4\pi k_0^2 k^2}\left[-k_1 k_{30} + \left(k_1^2 + k_2^2\right)\zeta_1\right], \tag{125}$$

$$\Phi_{23}(\mathbf{k}) = \frac{E(k_0)}{4\pi k_0^2 k^2}\left[-k_2 k_{30} + \left(k_1^2 + k_2^2\right)\zeta_2\right], \quad \text{and} \tag{126}$$

$$\Phi_{33}(\mathbf{k}) = \frac{E(k_0)}{4\pi k^4}\left(k_1^2 + k_2^2\right). \tag{127}$$

The *initial* (before the onset of shear distortion) wave number is

$$\mathbf{k}_0 = (k_1, k_2, k_{30}), \tag{128}$$

where

$$k_{30} = k_3 - \beta k_1. \tag{129}$$

The quantities ζ_i are given by the equations

$$\zeta_1 = C_1 - \frac{k_2}{k_1}C_2, \quad \zeta_2 = \frac{k_2}{k_1}C_1 + C_2, \tag{130}$$

where

$$C_1 = \frac{\beta k_1^2\left(k_0^2 - 2k_{30}^2 + \beta k_1 k_{30}\right)}{k^2\left(k_1^2 + k_2^2\right)}, \tag{131}$$

and

$$C_2 = \frac{k_2 k_0^2}{\left(k_1^2 + k_2^2\right)^{3/2}}\arctan\left[\frac{\beta k_1\left(k_1^2 + k_2^2\right)^{1/2}}{k_0^2 - \beta k_{30}k_1}\right]. \tag{132}$$

To facilitate implementation of Mann's model on a computer, rewriting the hypergeometric geometric function in equation (121) as an incomplete beta function is helpful. First, by applying equation (15.3.4) in Abramowitz and Stegun (1965), we have

$$_2F_1\left[\frac{1}{3}, \frac{17}{6}; \frac{4}{3}; -(k\ell)^{-2}\right] = \frac{(k\ell)^{2/3}}{(1 + k^2\ell^2)^{1/3}}\,_2F_1\left(\frac{1}{3}, -\frac{3}{2}; \frac{4}{3}; \frac{1}{1 + k^2\ell^2}\right).$$

Then, by applying Abramowitz and Stegun's equation (6.6.8) to the right-hand side, we have

$$_2F_1\left[\frac{1}{3},\frac{17}{6};\frac{4}{3};-(k\ell)^{-2}\right]=\frac{(k\ell)^{2/3}}{3}\,B_{1/(1+k^2\ell^2)}\left(\frac{1}{3},\frac{5}{2}\right).$$

Hence the nondimensional eddy lifetime can be expressed as

$$\beta=\frac{\sqrt{3}\Gamma}{k\ell}\left[B_{1/(1+k^2\ell^2)}\left(\frac{1}{3},\frac{5}{2}\right)\right]^{-1/2}. \tag{133}$$

The incomplete beta function (with argument in the domain $[0,1]$) can be computed using routines available with software packages such as Matlab.

8.3 Variances and Parameter Selection

The variances and covariances in the Mann model can be found by numerically integrating the 3D spectra $\Phi_{ij}(\mathbf{k})$, in accordance with equation (9). The results, as a function of Γ, are shown in figure 13. As Γ is increased, the variance in the streamwise component σ_{11}^2 increases. So too does the cross-stream variance σ_{22}^2 increase, although at a lesser rate. The vertical variance σ_{33}^2 decreases slightly. Note also that the model predicts a negative covariance σ_{13}^2 between the streamwise and vertical fluctuations, which is an important intrinsic feature of a shear layer. (All of the models discussed earlier were somewhat unrealistic in that they predict zero σ_{13}^2.)

It is also interesting to look at the integral length scales as a function of Γ. These are shown in figure 14. (The computation involved performing the integration in eq (12) numerically and then applying eq (18).) When $\Gamma = 0$, we have the usual result for isotropic turbulence that the longitudinal integral length scales (e.g., $L_{11,1}$) are twice the transverse scales (e.g., $L_{22,1}$ and $L_{33,1}$). All of the integral length scales shown initially increase with increasing Γ, although for $\Gamma > 1.5$, $L_{33,1}$ starts to decline.

Mann chose the model parameters using a least-squares method formulated to give the best fit with 1D spectra. In this report, I used a somewhat simpler method that gives similar results. The main idea is to choose Γ to match the ratio $\sigma_{11}^2/\sigma_{33}^2$ measured by Kaimal *et al.* From table 1, this ratio should be $4.77/1.46 = 3.27$. Using the data shown in figure 13, one can show the value of Γ that produces this ratio to be $\Gamma = \Gamma_0 = 3.53$. Since Mann (1994) found his atmospheric data were best described by values for Γ in the range of 2.5 to 3.5, the value suggested appears reasonable.
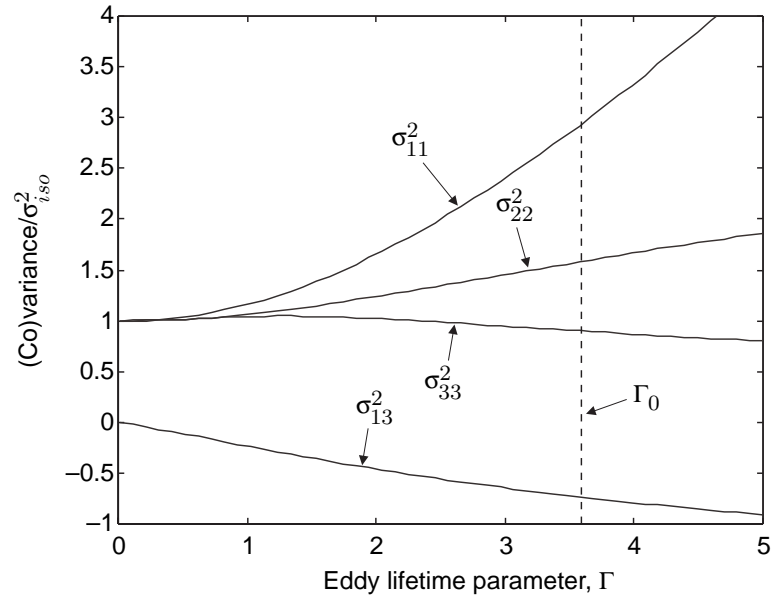
Figure 13. Variances of three velocity components and covariance between longitudinal and vertical velocities, according to Mann model. (Co)variances are plotted as a function of Γ, a parameter controlling eddy lifetime.
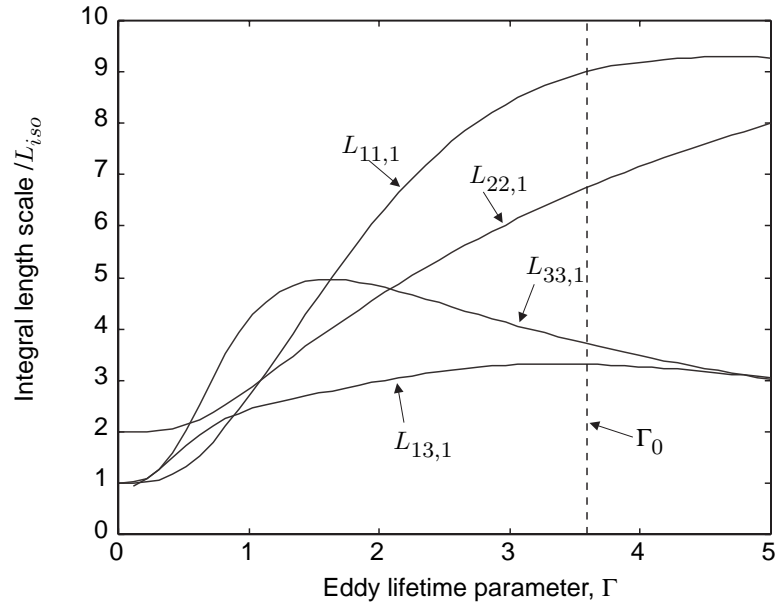

Figure 14. Integral length scales for three velocity components and for joint fluctuations between longitudinal and vertical velocities, according to Mann model. Length scales are plotted as a function of Γ, a parameter controlling eddy lifetime.

To force σ_{11}^2 equal to $4.77u_*^2$ when $\Gamma = \Gamma_0$, we need to set

$$\sigma_{iso}^2 = 1.88u_*^2 \tag{134}$$

in the initial von Kármán spectrum.

In order to reproduce the inertial-subrange asymptote, we must set

$$\ell = \left[\frac{2\Gamma(5/6)\sigma_{iso}^2}{\sqrt{\pi}\Gamma(1/3)\alpha_1} \right]^{3/2} \frac{1}{\epsilon} = 0.805z. \tag{135}$$

8.4 2D Correlation Functions

The 2D correlation functions for the Mann model can be found using equation (14). Since $\Phi_{ii}(\mathbf{k}_\perp)$ depends on the orientation of $\mathbf{k}_\perp$, the double integral cannot be reduced to a single one involving a Bessel function as in equation (46). However, if we are interested in sensor separations along just one of the orthogonal coordinate axes, equation (14) can be simplified somewhat. For example,

$$b_{11,1}(r_2, 0) = \int_{-\infty}^{\infty} \left[\int_{-\infty}^{\infty} \Phi_{11}(0, k_2, k_3) \, dk_3 \right] \exp(ik_2 r_2) \, dk_2, \tag{136}$$

or

$$b_{11,1}(0, r_3) = \int_{-\infty}^{\infty} \left[\int_{-\infty}^{\infty} \Phi_{11}(0, k_2, k_3) \, dk_2 \right] \exp(ik_3 r_3) \, dk_3. \tag{137}$$

The advantage of these equations is that the full Fourier transform needs to be performed along just one axis. A simple numerical integration can be performed along the other axis. Note that the 2D structure functions in the Mann model depend on the direction of the displacement. This distinguishes the Mann model from the ones considered earlier.

Predictions of the 2D structure function for the Mann model are shown in figures 11 to 12. Note that the structure functions for both horizontal and vertical separations are nearly the same for small separations compared to the height (the inertial subrange), diverge for moderate separations, and then become equal for large separations. The reason why they become equal for large separations is that $b_{11,1}(r, 0)$ and $b_{11,1}(0, r)$ both approach zero for large r, so that the 2D structure function in the two cases is $d_{11,1}(r, 0) \simeq d_{11,1}(0, r) \simeq 2b_{11,1}(0, 0)$. For large separations, the enhancement of the along-wind structure function $d_{11,1}$ predicted by the Mann model is about half that predicted by the Kristensen *et al* model. The predictions differ even more in the crosswind direction: the Mann model predictions for $d_{22,2}$ are about $1/10$ the Kristensen *et al* predictions.

9. Anisotropy and the Coherence of Sound Waves

So far in this report, I have dealt only with the modeling of anisotropic turbulence, without discussing its significance to wave propagation. The effect of anisotropic turbulence on the coherence of a propagating sound wave will be discussed in this section.

9.1   Mutual Coherence Function

The MCF describes the coherence between a pair of sensors as a function of their separation $\mathbf{r}$, normal to the direction of propagation. It is given by (Wilson, 1997a)

$$\Gamma\left(\mathbf{r}\right) = \exp\left[-\frac{\pi}{4}Rk^2 d_u\left(\mathbf{r}\right)\right], \tag{138}$$

where R is the propagation distance (range); $k = 2\pi f/c_0$ the wavenumber, f the frequency, c_0 the sound speed; and $d_u\left(\mathbf{r}\right)$ the 2D structure function of the effective index-of-refraction fluctuations. The function $d_u\left(\mathbf{r}\right)$ is related to its counterpart for the velocity fluctuations according to (Wilson, 1997a)

$$d_u\left(\mathbf{r}_\perp\right) = \frac{4}{c_0^2}d_{ii,i}\left(\mathbf{r}_\perp\right), \tag{139}$$

where the direction of propagation is the ith axis, and $\mathbf{r}_\perp$ is a displacement perpendicular to the ith axis.

In the shear-layer models considered in this report, all of the variances scale in proportion to u_*^2, and all of the length scales to z. From equations (13) and (15), we see that $d_{ii,i}\left(\mathbf{r}_\perp\right)$ is proportional to zu_*^2. Hence let us define the nondimensionalized 2D velocity structure function as

$$\overline{d}_{ii,i}\left(\mathbf{r}_\perp\right) = \frac{d_{ii,i}\left(\mathbf{r}_\perp\right)}{zu_*^2}. \tag{140}$$

Substituting equation (139) into (140) and the result into (138), we have

$$\Gamma\left(\mathbf{r}\right) = \exp\left[-\frac{\pi}{4}\overline{R}\,\overline{d}_{ii,i}\left(\mathbf{r}\right)\right], \tag{141}$$

where

$$\overline{R} = \frac{4Rk^2 zu_*^2}{c_0^2}. \tag{142}$$

Hence, by plotting the MCF as a function of the normalized range $\overline{R}$ and normalized separation $\mathbf{r}/z$, we can generate universal sets of curves scalable to arbitrary values of the range, sensor separation, frequency, height, friction velocity, and sound speed.

The dependence of the MCFs on the normalized range, for the Kolmogorov model, various von Kármán models, and the Kristensen *et al* model, is plotted in figures 15 to 18. The first two plots show along-wind MCFs for sensor separations equal to 0.1 and 1 times the height; the second two are the corresponding crosswind plots. When $r/z = 0.1$, the various models agree fairly well. The MCF for the Kolmogorov model is only slightly less than the others. The differences become more pronounced when $r/z = 1$. At this separation, the Kolmogorov model predicts much lower coherence than the others. Also, the isotropic von Kármán model predicts a coherence that is too high in the along-wind direction.

A similar set of comparisons, this time with the Kolmogorov, Gaussian, Kristensen *et al*, and Mann models, is shown in figures 19 to 22. When $r/z = 0.1$, the predicted coherence from the Gaussian model is much too high. This is because the Gaussian model does not have a realistic inertial subrange. The Gaussian model works well when $r/z = 1$, though. MCFs from the Kristensen *et al* and Mann models agree reasonably well, although for crosswind propagation when $r/z = 1$, the Mann model predicts significantly higher coherence.
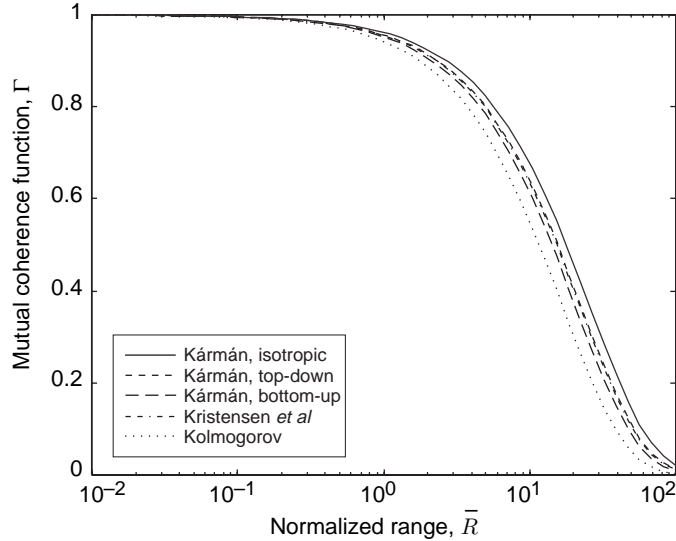

Figure 15. MCF as a function of normalized range, for Kolmogorov, various von Kármán, and Kristensen *et al* models. Propagation is along wind. Sensor separation is 0.1 times height.
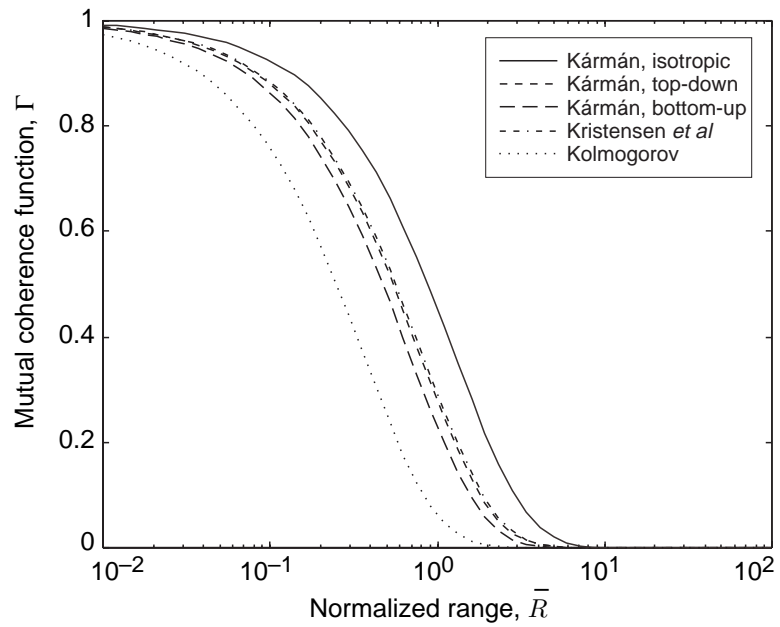
Figure 16. MCF as a function of normalized range, for Kolmogorov, various von Kármán, and Kristensen *et al* models. Propagation is along wind. Sensor separation equals height.
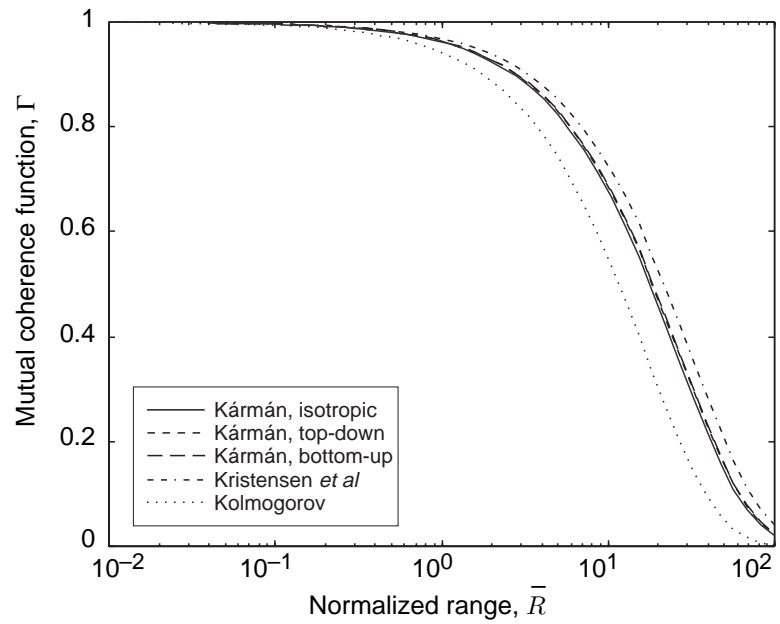

Figure 17. MCF as a function of normalized range, for Kolmogorov, various von Kármán, and Kristensen *et al* models. Propagation is crosswind. Sensor separation is 0.1 times height.
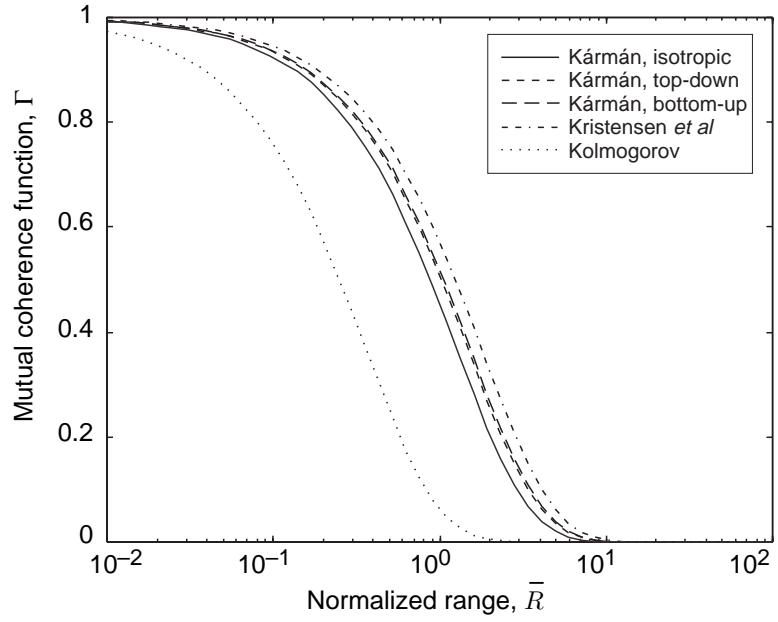
Figure 18. MCF as a function of normalized range, for Kolmogorov, various von Kármán models, and Kristensen *et al* models. Propagation is crosswind. Sensor separation equals height.
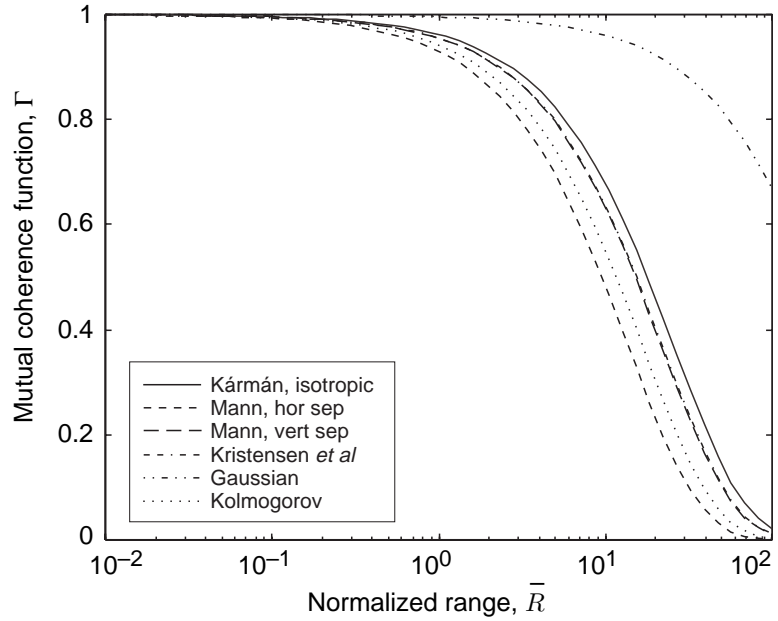

Figure 19. MCF as a function of normalized range, for Kolmogorov, isotropic von Kármán, Gaussian, Kristensen *et al*, and Mann models. Propagation is along wind. Sensor separation is 0.1 times height.

Figure 20. MCF as a function of normalized range, for Kolmogorov, isotropic von Kármán, Gaussian, Kristensen *et al*, and Mann models. Propagation is along wind. Sensor separation equals the height.
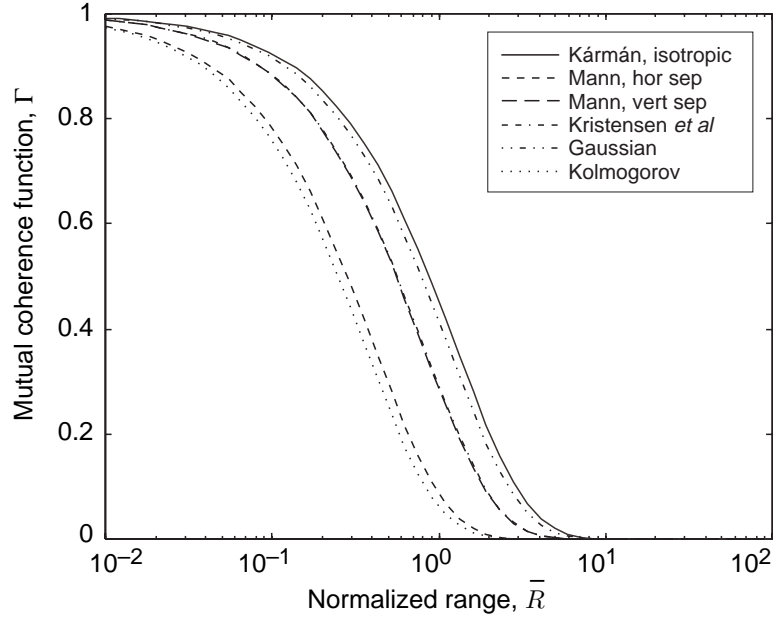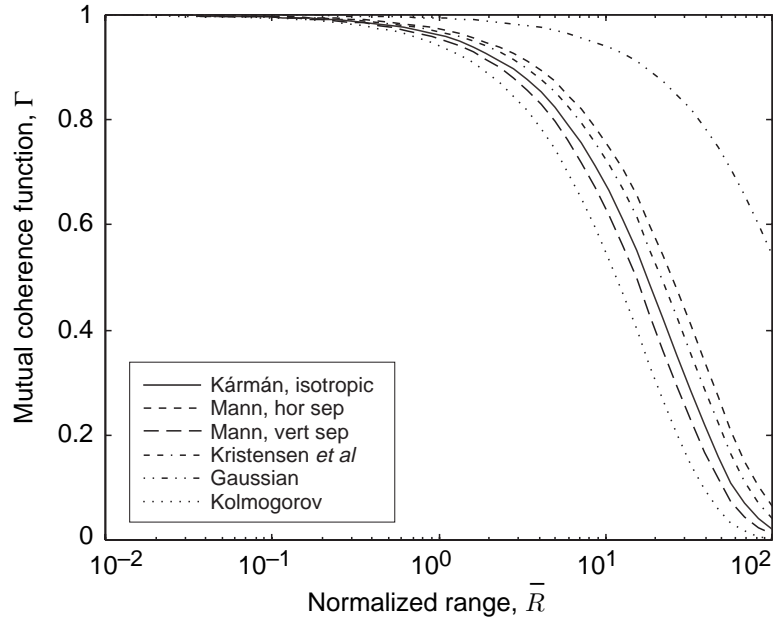

Figure 21. MCF as a function of normalized range, for Kolmogorov, isotropic von Kármán, Gaussian, Kristensen *et al*, and Mann models. Propagation is crosswind. Sensor separation is 0.1 times height.
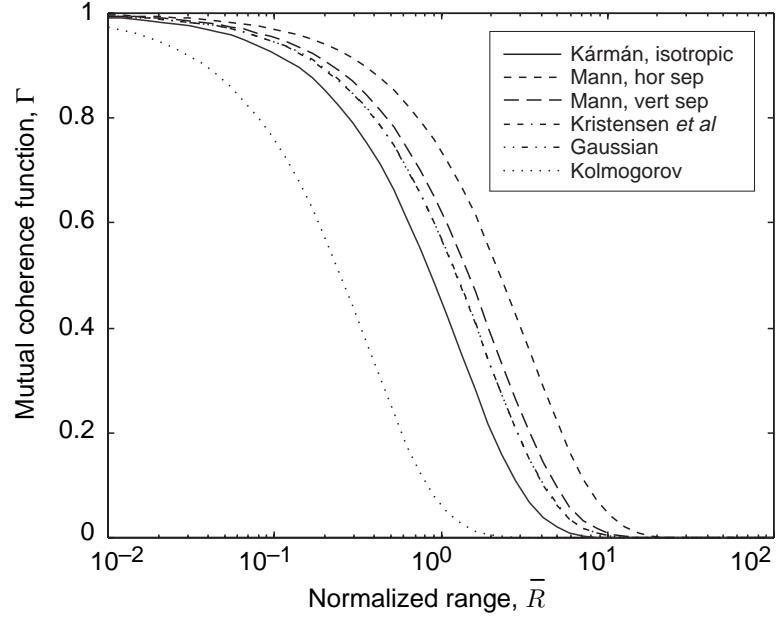
48

Figure 22. MCF as a function of normalized range, for Kolmogorov, isotropic von Kármán, Gaussian, Kristensen *et al*, and Mann models. Propagation is crosswind. Sensor separation equals height.

9.2 Performance of Acoustic Direction-Finding Arrays

An important application of the theory of mutual coherence is the prediction of source direction-finding accuracy from acoustical arrays. A full treatment of this problem was provided by Wilson (1997a). The procedure described in that report involved calculating the *Cramer-Rao lower bound* (CRLB) corresponding to a given array configuration, turbulence model, and noise environment. The CRLB is the standard deviation in the wavefront angle-of-arrival estimates about their actual value attained using an ideal estimation method.[*] Or more simply put, when the CRLB is equal to α degrees, we can usually measure the direction of a source to an accuracy of α degrees, if equipment and processing methods are good.

Actual CRLB calculations, for many of the models discussed earlier in this report, are shown in figures 23 to 30. The calculations were performed for a six-element array, with the sensors evenly spaced around a horizontal circle having a radius of 1.2 m. It turns out that the CRLB for such an array configuration is independent of the source direction (Wilson, 1997a). The

---

[*]The CRLB is strictly the variance of the estimates, not their standard deviation (square root of the variance). Because the standard deviation has linear units and is therefore more natural to deal with, however, I have adopted the implicit convention of meaning the square root of the CRLB whenever I refer to the CRLB throughout this report.

source and array heights were both 1 m, the friction velocity was $u_* = 0.5$ m/s (windy conditions), the SNR was 20 dB, and five statistically independent measurements were used for each angle-of-arrival estimate. The plots show the dependence of the CRLB for horizontal bearings on source range (propagation distance) and frequency.

The general appearance of the CRLB plots, for all of the models, is similar. Near the source and at low frequency, the CRLB is independent of range. This independence is because the main determinant of array performance near the source is the environmental noise. As the frequency and range are increased, however, the CRLB contours turn upward dramatically. Within this region, distortion of the wavefronts by turbulence begins to be the most significant determinant of array performance.

The Kolmogorov model (fig. 23) predicts higher values for the CRLB than the other models, particularly at lower frequencies and longer ranges. The reason is that the Kolmogorov model predicts too much energy at the large scales, which are most important in determining the array performance. Therefore the Kolmogorov model should be avoided in this application. CRLB predictions for the isotropic von Kármán model (fig. 24) agree reasonably well with calculations from the more complicated, anisotropic models (figs. 25 to 30). Its predictions fall midway between the along-wind and crosswind predictions of the Kristensen *et al* (figs. 26 to 27) and Mann
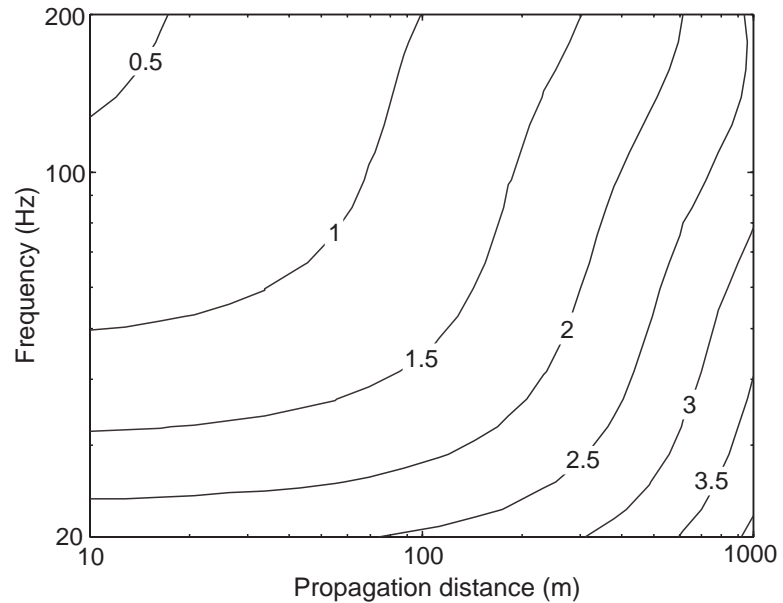

Figure 23. CRLB calculations for Kolmogorov inertial-subrange model.
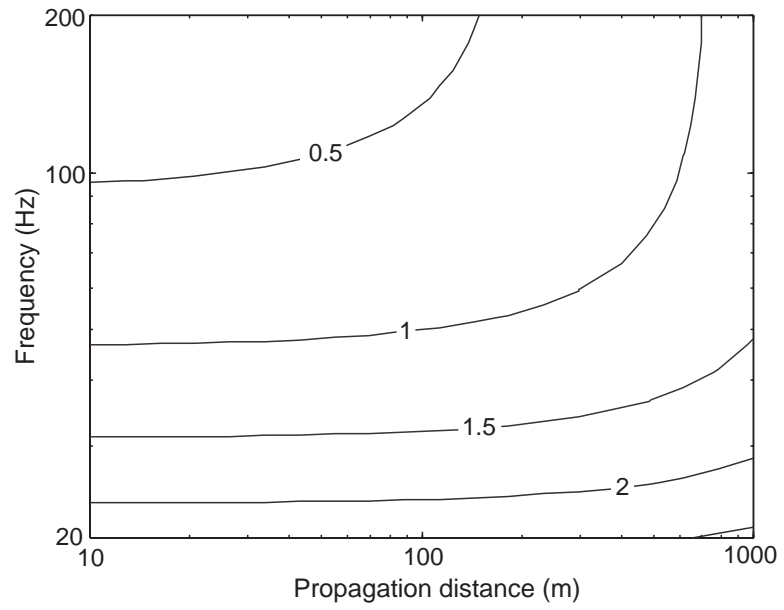
Figure 24. CRLB calculations for isotropic von Kármán model.

Figure 25. CRLB calculations for anisotropic bottom-up von Kármán model, for propaga-
tion in along-wind direction.

Figure 26. CRLB calculations for Kristensen *et al* model, for propagation in along-wind direction.

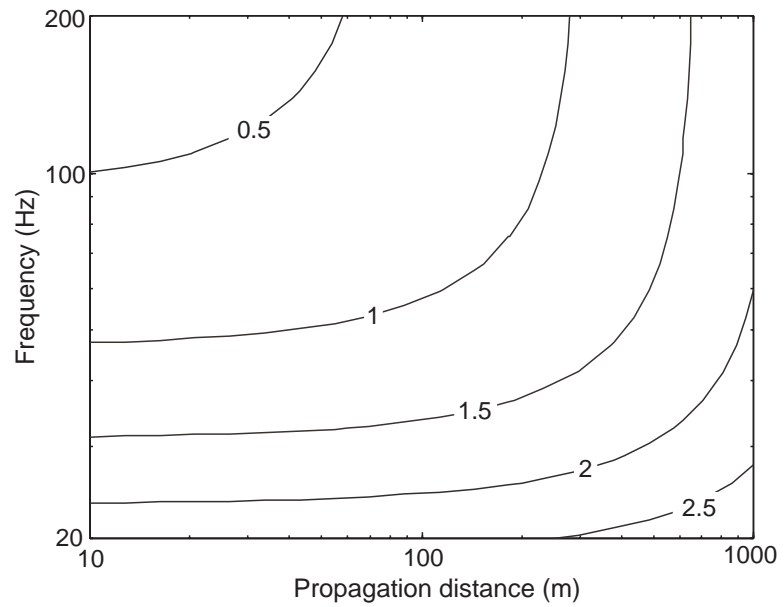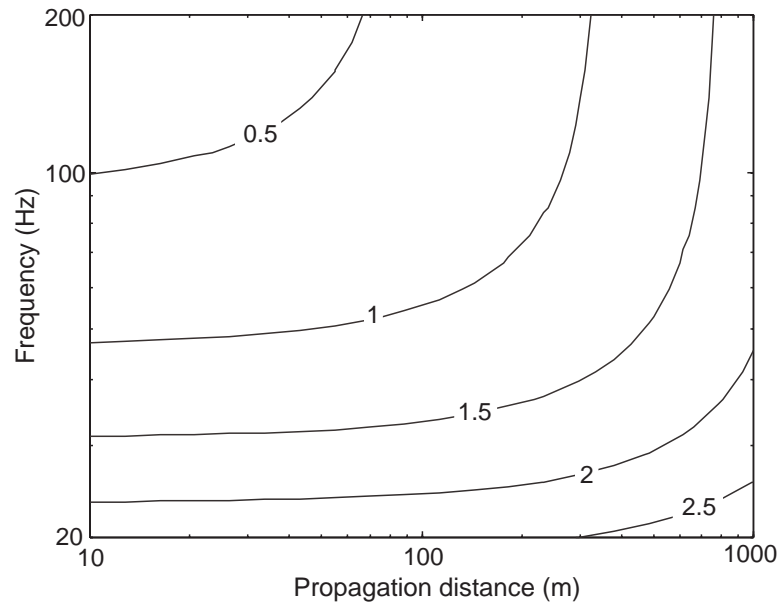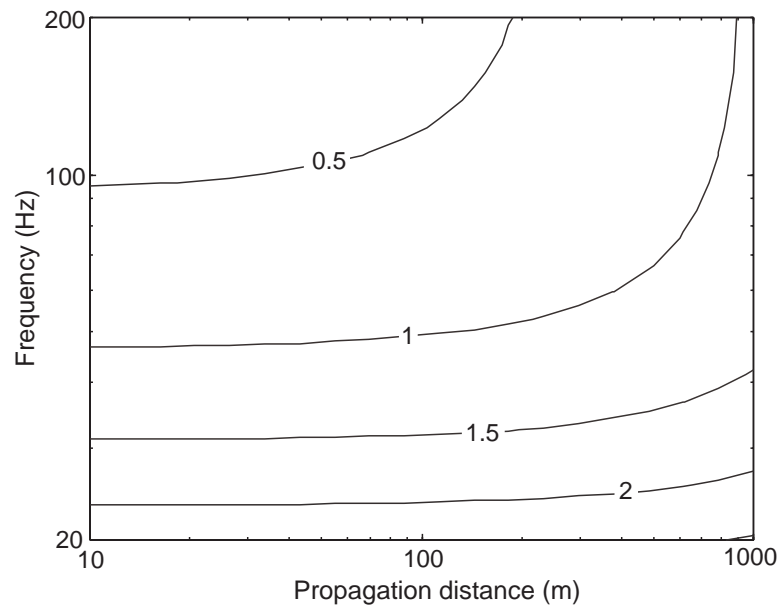Figure 27. CRLB calculations for Kristensen *et al* model, for horizontal propagation in crosswind direction.
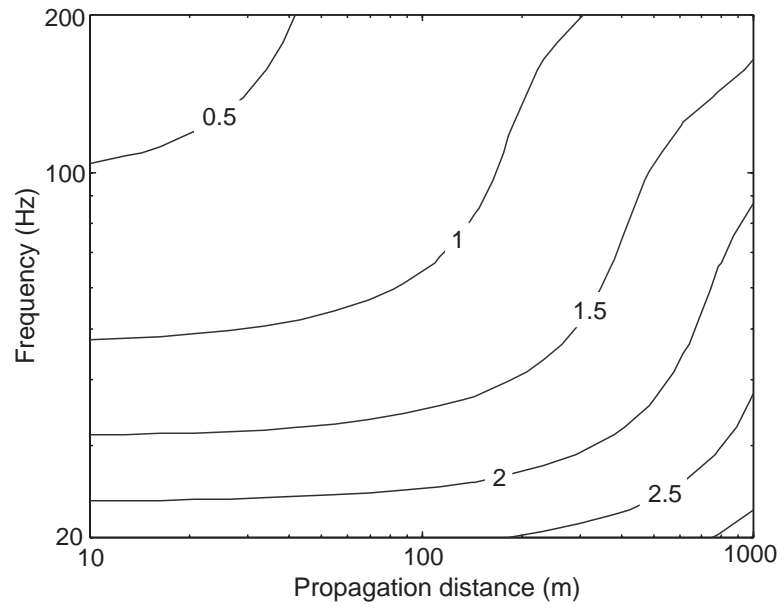
Figure 28. CRLB calculations for bottom-up anisotropic Gaussian model, for propagation in along-wind directions.
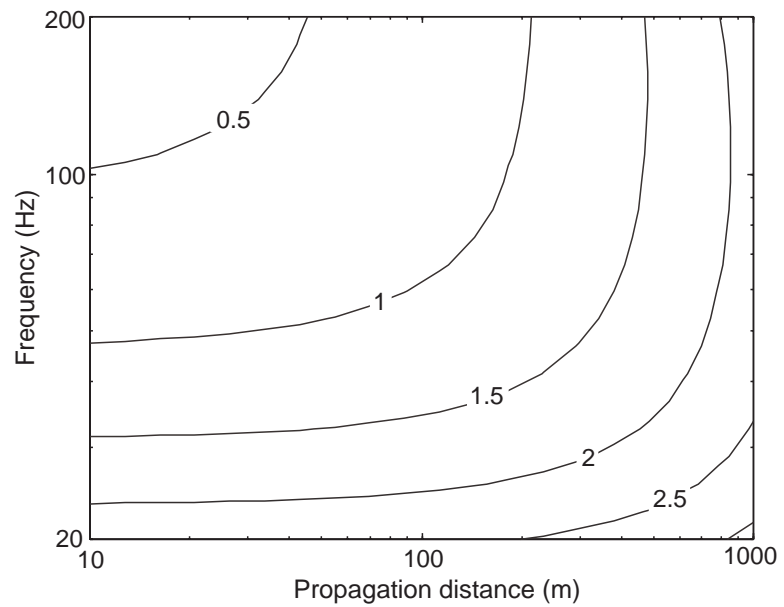

Figure 29. CRLB calculations for Mann model, for propagation in along-wind direction.
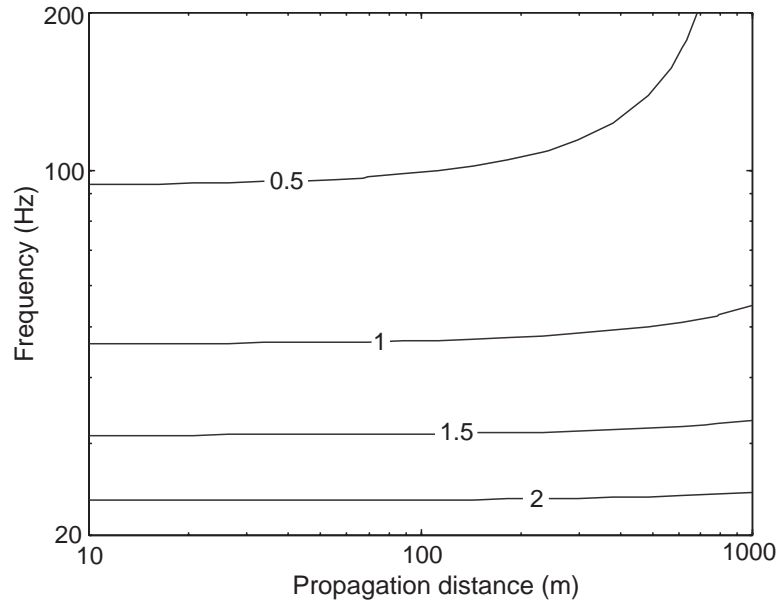
Figure 30. CRLB calculations for Mann model, for horizontal propagation in crosswind direction.

(figs. 29 to 30) models. Predictions from the bottom-up von Kármán model, in the along-wind direction (fig. 25), are close to the corresponding predictions for the Kristensen *et al* (fig. 26) and Mann (fig. 29) models. The bottom-up Gaussian model, in the along-wind direction (fig. 28), also agrees well with the corresponding predictions from the Kristensen *et al* and Mann models, although the contours start to diverge for high frequencies and long propagation distances. This may be due to the inability of the Gaussian model to realistically capture small-scale turbulence structure.

The Kristensen *et al* and Mann models are probably the most realistic, and agree in most regards. Interestingly, the anisotropic effect predicted by the Mann model is more pronounced than the effect predicted by the Kristensen *et al* model. In the along-wind direction, the Mann model (fig. 29) predicts higher CRLB than the Kristensen *et al* model (fig. 26); in the crosswind direction, it predicts lower CRLB (figs. 27 and 30).

On the basis of the CRLB calculations, we are led to the following conclusions:

1. The Kolmogorov model does not work very well for low-frequency acoustics and should therefore be avoided.

2. The isotropic von Kármán model is a convenient and reasonably accurate model for rough calculations.

3. The anisotropic versions of the von Kármán and Gaussian models have little practical value. If one is willing to go through the effort of using an anisotropic von Kármán or Gaussian model, it would be worthwhile to take the small additional step to the Kristensen *et al* model, or even consider using the Mann model.

10. Concluding Remarks

The assumption of isotropic turbulence is a common one and a reasonable starting point for creating statistical turbulence models. Previous researchers have used this assumption to derive equations for the second-order statistics needed in wave propagation calculations. By starting with a Gaussian-type equation for the correlation function, for example, or with a von Kármán-type equation for the energy spectrum, one can use well-known relationships for isotropic homogeneous turbulence to derive any other second-order statistics of interest.

The main motivation for selecting the isotropic Gaussian and von Kármán models (as opposed to Kolmogorov's inertial-subrange model) is that they are well-behaved for the large-scale, energy subrange turbulence. This large-scale turbulence is important in low-frequency acoustics. Although the isotropic Gaussian and von Kármán models are more satisfactory for large-scale turbulence than the Kolmogorov model, they are still unrealistic in one critical aspect: they neglect anisotropy of the large-scale turbulence.

My main intention in this report was to remedy this problem, by showing how anisotropic versions of the Gaussian and von Kármán models can be built. This task proved surprisingly difficult. Even though a simple, idealized form of anisotropy was assumed (eq (23)), the mathematical development of the models quickly became complex. Difficulties in deriving closed-form equations for statistical quantities of interest, such as the 2D correlation functions, made numerical integrations necessary.

The inherent complexity of even "simple" anisotropic models with obvious shortcomings (such as those developed based on eq (23)) makes their direct application unappealing. In practice it is probably not much more difficult to use the first-principle model developed by Mann (1994).

This report has featured extensive comparisons between different statistical turbulence models, with and without anisotropy. Although such comparisons are a helpful first step toward understanding the effects of anisotropic turbulence on acoustic propagation, in the end experiments are needed to test how well the various anisotropic models actually work for predicting acoustic propagation characteristics. Such experiments are left for future research.

Appendix A.   Some Useful Integrals

Several solutions to integrals that were used in the body of this report are provided in this appendix, along with citations of their sources.

1. From Beyer (1981), definite integral equation (615),

$$\int_0^\infty \frac{x^{n-1}\,dx}{(1+x^2)^\nu} = \frac{\Gamma(n/2)\,\Gamma(\nu-n/2)}{2\Gamma(\nu)} = \frac{1}{2}B(n/2, \nu-n/2). \quad \text{(A-1)}$$

By changing the variable of integration from x to $y = cx/a$ in the above equation and setting $n = 2m + 2$, one arrives at the useful equation

$$\int_0^\infty \frac{y^{2m+1}\,dy}{(c+ay^2)^\nu} = \frac{\Gamma(m+1)\,\Gamma(\nu-m-1)}{2\Gamma(\nu)\,a^{m+1}c^{\nu-m-1}} = \frac{1}{2a^{m+1}c^{\nu-m-1}}B(m+1, \nu-m-1). \quad \text{(A-2)}$$

2. From Gradshteyn and Ryzhik (1994), equation (6.565.4),

$$\int_0^\infty \frac{x^{\nu+1}}{(a^2+x^2)^{\mu+1}}J_\nu(bx)\,dx = \frac{a^{\nu-\mu}b^\mu}{2^\mu\Gamma(\mu+1)}K_{\nu-\mu}(ab). \quad \text{(A-3)}$$

3. From Gradshteyn and Ryzhik, equation (3.194.1),

$$\int_0^s \frac{t^{\nu+\varepsilon-3}}{(t/\ell^2+1)^\nu}dt = \frac{s^{\nu+\varepsilon-2}}{\nu+\varepsilon-2}\,_2F_1\left(\nu, \nu+\varepsilon-2; \nu+\varepsilon-1; -\frac{s}{\ell^2}\right), \quad \text{(A-4)}$$

where $_2F_1$ is the hypergeometric function. Actually, the integral can be rewritten in terms of an incomplete beta function rather than the hypergeometric function. This is convenient, since many software packages such as Matlab have routines for calculating incomplete beta functions, but not hypergeometric functions. It should be pointed out that these routines usually require that the argument to the incomplete beta function is in the range $[0, 1]$; hence we must try to recast our result in a form satisfying this requirement. Let us begin by substituting $u = t/\ell^2$ into the right-hand side of equation (A-4). We find

$$\int_0^s \frac{t^{\nu+\varepsilon-3}}{(t/\ell^2+1)^\nu}dt = \ell^{2(\nu+\varepsilon-2)}\int_0^{s/\ell^2} \frac{u^{\nu+\varepsilon-3}}{(u+1)^\nu}du. \quad \text{(A-5)}$$

Next we adopt a trick from Kristensen *et al* (1989) by setting $\eta = u/(1+u)$, with result

$$\int_0^s \frac{t^{\nu+\varepsilon-3}}{(t/\ell^2+1)^\nu} dt = \ell^{2(\nu+\varepsilon-2)} \int_0^{s/\ell^2/(1+s/\ell^2)} \eta^{\nu+\varepsilon-3} (1-\eta)^{1-\varepsilon} d\eta. \qquad \text{(A-6)}$$

From the definition of the incomplete beta function (eq (84)), we have

$$\int_0^s \frac{t^{\nu+\varepsilon-3}}{(t/\ell^2+1)^\nu} dt = \ell^{2(\nu+\varepsilon-2)} B_{s/\ell^2/(1+s/\ell^2)}(\nu+\varepsilon-2, 2-\varepsilon). \qquad \text{(A-7)}$$

Furthermore, setting $s = k^{-2}$, we can write this as

$$\int_0^{k^{-2}} \frac{t^{\nu+\varepsilon-3}}{(t/\ell^2+1)^\nu} dt = \ell^{2(\nu+\varepsilon-2)} B_{1/(1+k^2\ell^2)}(\nu+\varepsilon-2, 2-\varepsilon). \qquad \text{(A-8)}$$

Note that for all real values of k, the argument to the beta function, $1/(1+k^2\ell^2)$, is indeed in the range $[0, 1]$.

4. From Gradshteyn and Ryzhik, equation (3.381.3),

$$\int_u^\infty x^{\nu-1} e^{-\mu x} dx = \mu^{-\nu} \Gamma(\nu, \mu u),$$

where $\Gamma(x, y)$ is the incomplete gamma function. When we substitute, $t = 1/x$, and $s = 1/u$, the integral becomes

$$\int_0^s t^{-\nu-1} e^{-\mu/t} dt = \mu^{-\nu} \Gamma\left(\nu, \frac{\mu}{s}\right). \qquad \text{(A-9)}$$

5. In order to calculate the 2D correlation function for the bottom-up von Kármán model, one must solve integrals of the form

$$I = \int_0^\infty \left(k^2\ell^2\right)^{-q} B_{1/(1+k^2\ell^2)}(a, b) J_0(kr) k \, dk. \qquad \text{(A-10)}$$

It happens that these integrals can be determined in terms of Meijer's G-functions. We begin by writing the incomplete beta function as a hypergeometric function using equation (6.6.8) from Abramowitz and Stegun (1965):

$$B_{1/(1+k^2\ell^2)}(a, b) = a^{-1} \left(\frac{1}{1+k^2\ell^2}\right)^a F\left(a, 1-b; a+1; \frac{1}{1+k^2\ell^2}\right).$$

Next, we transform the hypergeometric function using equation (15.3.4) from Abramowitz and Stegun:

$$B_{1/(1+k^2\ell^2)}(a,b) = a^{-1}\left(k^2\ell^2\right)^{-a} F\left(a, a+b; a+1; -\frac{1}{k^2\ell^2}\right).$$

The hypergeometric function can now be recast as a Meijer's G-function, using equations (9.34.7) and (9.31.2) from Gradshteyn and Ryzhik (1994). The result is

$$B_{1/(1+k^2\ell^2)}(a,b) = \frac{\left(k^2\ell^2\right)^{-a-1}}{\Gamma(a+b)} G_{22}^{21}\left(k^2\ell^2 \left|\begin{array}{c} 2,\ a+2 \\ a+1,\ a+b+1 \end{array}\right.\right). \tag{A-11}$$

We can now substitute equation (A-11) into (A-10) and solve the integral using equation (7.822.1) from Gradshteyn and Ryzhik (1994). The result is

$$I = \frac{1}{2\ell^2\Gamma(a+b)}\left(\frac{r}{2\ell}\right)^{2q+2a} G_{42}^{22}\left(\frac{4\ell^2}{r^2} \left|\begin{array}{c} a+q+1,\ 2,\ a+2,\ a+q+1 \\ a+1,\ a+b+1 \end{array}\right.\right). \tag{A-12}$$

Bibliography

Abramowitz, M. and I. A. Stegun (1965): *Handbook of Mathematical Functions*. Dover, San Francisco, 675–679.

Batchelor, G. K. (1953): *The Theory of Homogeneous Turbulence*. Cambridge Univ. Press, Cambridge, Great Britain.

Beyer, W. H., editor (1981): *CRC Standard Mathematical Tables*. CRC Press, Boca Raton, Florida, twenty-fifth edition.

Gradshteyn, I. S. and I. M. Ryzhik (1994): *Table of Integrals, Series, and Products*. Academic Press, San Diego.

Kaimal, J. C., J. C. Wyngaard, Y. Izumi, and O. R. Coté (1972): Spectral characteristics of surface layer turbulence. *Q. J. R. Meteorol. Soc.*, **98**, 563–589.

Kolmogorov, A. N. (1941): The local structure of turbulence in incompressible viscous fluid for very large Reynolds numbers. *C. R. Acad. Sci. URSS*, **30**, 301–305.

Krasnenko, N. P., A. L. Afanas'ev, and A. P. Rostov (1997): Spatial-temporal structure of fluctuations of the amplitude and phase of acoustical wave propagating through the atmospheric boundary layer, 3rd interim report. Contractor Report N 68171–96–C–9067, U.S. Naval Regional Contracting Detachment London DoE Complex, Block 2, Wing 11, Eastcote Road RuiSlip, MIDDX, United Kingdom, HA4 8BS.

Kristensen, L., D. H. Lenschow, P. Kirkegaard, and M. Courtney (1989): The spectral velocity tensor for homogeneous boundary-layer turbulence. *Bound. Layer Meteor.*, **47**, 149–193.

Mann, J. (1994): The spatial structure of neutral atmospheric surface layer turbulence. *J. Fluid Mech.*, **273**, 141–168.

Panofsky, H. A. and J. A. Dutton (1984): *Atmospheric Turbulence: Models and Methods for Engineering Applications*. Wiley & Sons, New York.

Stull, R. B. (1988): *An Introduction to Boundary Layer Meteorology*. Kluwer, Dordrecht, Germany.

Tatarskii, V. I. (1971): *The Effects of the Turbulent Atmosphere on Wave Propagation*. Keter, Jerusalem.

Wilson, D. K. (1997a): Performance of acoustic tracking arrays in atmospheric turbulence. Technical Report ARL-TR-1286, U.S. Army Research Laboratory, 2800 Powder Mill Road, Adelphi, MD 20783.

Wilson, D. K. (1997b): Three-dimensional correlation and spectral functions for turbulent velocities in homogeneous and surface-blocked boundary layers. Technical Report ARL-TR-1287, U.S. Army Research Laboratory, 2800 Powder Mill Road, Adelphi, MD 20783.

Wyngaard, J. C. and R. A. Brost (1984): Top-down and bottom-up diffusion of a scalar in the convective boundary layer. *J. Atmos. Sci.*, **41**, 102–112.

Distribution

blank

blank

blank

Report Documentation Page

Distribution

Admnstr
Defns Techl Info Ctr
Attn DTIC-OCP
8725 John J Kingman Rd Ste 0944
FT Belvoir VA 22060-6218

Mil Asst for Env Sci
Ofc of the Undersec of Defns for Rsrch &
  Engrg R&AT E LS
Pentagon Rm 3D129
Washington DC 20301-3080

Ofc of the Dir Rsrch and Engrg
Attn R Menz
Pentagon Rm 3E1089
Washington DC 20301-3080

Ofc of the Secy of Defns
Attn ODDRE (R&AT) G Singley
Attn ODDRE (R&AT) S Gontarek
The Pentagon
Washington DC 20301-3080

OSD
Attn OUSD(A&T)/ODDDR&E(R) J Lupo
Washington DC 20301-7100

ARL Chemical Biology Nuc Effects Div
Attn AMSRL-SL-CO
Aberdeen Proving Ground MD 21005-5423

Army Communications Elec Ctr for EW
  RSTA
Attn AMSEL-EW-D
FT Monmouth NJ 07703-5303

Army Corps of Engrs Engr Topographics Lab
Attn ETL-GS-LB
FT Belvoir VA 22060

Army Dugway Proving Ground
Attn STEDP 3
Attn STEDP-MT-DA-L-3
Attn STEDP-MT-M   Bowers
Dugway UT 84022-5000

Army Field Artillery School
Attn ATSF-TSM-TA
FT Sill OK 73503-5000

Army Foreign Sci Tech Ctr
Attn CM
220 7th Stret NE
Charlottesville VA 22901-5396

Army Infantry
Attn ATSH-CD-CS-OR E Dutoit
FT Benning GA 30905-5090

Army Materiel Sys Analysis Activity
Attn AMXSY-AT   Campbell
Attn AMXSY-CS   Bradley
Aberdeen Proving Ground MD 21005-5071

Army Missile Cmnd
Attn AMSMI-RD-AC-AD   Peterson
Redstone Arsenal AL 35898-5242

Army Missile Cmnd
Attn AMSMI-RD-DE-SE G Lill Jr
Redstone Arsenal AL 35898-5245

Army Missile Cmnd
Attn AMSMI-RD-AS-SS R Alongi
Redstone Arsenal AL 35898-5253

Army Rsrch Ofc
Attn AMXRO-GS   Bach
PO Box 12211
Research Triangle Park NC 27709

Army Strat Defns Cmnd
Attn CSSD-SL-L   Lilly
PO Box 1500
Huntsville AL 35807-3801

Army TACOM-ARDEC
Attn AMSTA-AR-WEL-TL
Bldg 59 Phillips Rd
Picatinny Arsenal NJ 07806-5000

CECOM
Attn PM GPS COL S Young
FT Monmouth NJ 07703

CECOM RDEC Elect System Div Dir
Attn J Niemela
FT Monmouth NJ 07703

CECOM
Sp & Terrestrial Commctn Div
Attn AMSEL-RD-ST-MC-M H Soicher
FT Monmouth NJ 07703-5203

Dir of Assessment and Eval
Attn SARD-ZD H K Fallin Jr
103 Army Pentagon Rm 2E673
Washington DC 20301-0163

Dpty Assist Secy for Rsrch & Techl
Attn SARD-TT F Milton Rm 3E479
The Pentagon
Washington DC 20301-0103

Hdqtrs Dept of the Army
Attn DAMO-FDT D Schmidt
400 Army Pentagon Rm 3C514
Washington DC 20301-0460

MICOM RDEC
Attn AMSMI-RD W C McCorkle
Redstone Arsenal AL 35898-5240

Natl Security Agency
Attn W21   Longbothum
9800 Savage Rd
FT George G Meade MD 20755-6000

TACOM
Attn AMSTA-TR-R E Shalis
Mail Stop 263
Warren MI 48090

US Army ARDEC
Attn AMSTA-AR-FSF-RM J Heberley
Bldg 95N
Picatinny Arsenal NJ 07806

US Army Avn Rsrch, Dev, & Engrg Ctr
Attn T L House
4300 Goodfellow Blvd
St Louis MO 63120-1798

US Army CECOM Rsrch, Dev, & Engrg
Attn R F Giordano
FT Monmouth NJ 07703-5201

US Army Edgewood Rsrch, Dev, & Engrg Ctr
Attn SCBRD-TD J Vervier
Aberdeen Proving Ground MD 21010-5423

US Army Info Sys Engrg Cmnd
Attn ASQB-OTD F Jenia
FT Huachuca AZ 85613-5300

US Army Materiel Sys Analysis Activity
Attn AMXSY-CR   Marchetti
Attn AMXSY-D J McCarthy
Aberdeen Proving Ground MD 21005-5071

US Army Matl Cmnd
Dpty CG for RDE Hdqtrs
Attn AMCRD BG Beauchamp
5001 Eisenhower Ave
Alexandria VA 22333-0001

US Army Matl Cmnd
Prin Dpty for Acquisition Hdqrts
Attn AMCDCG-A D Adams
5001 Eisenhower Ave
Alexandria VA 22333-0001

US Army Matl Cmnd
Prin Dpty for Techlgy Hdqrts
Attn AMCDCG-T M Fisette
5001 Eisenhower Ave
Alexandria VA 22333-0001

 US Army Mis Cmnd (USAMICOM)
Attn AMSMI-RD-CS-R Documents
Redstone Arsenal AL 35898-5400

US Army Natick Rsrch, Dev, & Engrg Ctr
  Acting Techl Dir
Attn SSCNC-T P Brandler
Natick MA 01760-5002

US Army Nuclear & Chem Agency
Attn MONA-ZB
Bldg 2073
Springfield VA 22150-3198

US Army OEC
Attn CSTE-EFS
Park Center IV 4501 Ford Ave
Alexandria VA 22302-1458

US Army Rsrch Ofc
Attn G Iafrate
4300 S Miami Blvd
Research Triangle Park NC 27709

US Army Simulation, Train, & Instrmntn
  Cmnd
Attn J Stahl
12350 Research Parkway
Orlando FL 32826-3726

US Army Tank-Automtv & Armaments Cmnd
Attn AMSTA-AR-TD C Spinelli
Bldg 1
Picatinny Arsenal NJ 07806-5000

US Army Tank-Automtv Cmnd Rsrch, Dev, &
  Engrg Ctr
Attn AMSTA-TA J Chapin
Warren MI 48397-5000

US Army Test & Eval Cmnd
Attn R G Pollard III
Aberdeen Proving Ground MD 21005-5055

US Army TRADOC Anlys Cmnd—WSMR
Attn ATRC-WSS-R
White Sands Missile Range NM 88002

USATRADOC
Battle Lab Integration & Techl Dirctrt
Attn ATCD-B J A Klevecz
FT Monroe VA 23651-5850

US Military Academy
Dept of Mathematical Sci
Attn MAJ D Engen
West Point NY 10996

USAASA
Attn MOAS-AI W Parron
9325 Gunston Rd Ste N319
FT Belvoir VA 22060-5582

USACRREL
Attn CEREL-GP R Detsch
72 Lyme Rd
Hanover NH 03755-1290

USATRADOC
Attn ATCD-FA
FT Monroe VA 23651-5170

Nav Air War Cen Wpn Div
Attn CMD 420000D C0245 A Shlanta
1 Admin Cir
China Lake CA 93555-6001

Nav Surface Warfare Ctr
Attn Code B07 J Pennella
17320 Dahlgren Rd Bldg 1470 Rm 1101
Dahlgren VA 22448-5100

Naval Surface Weapons Ctr
Attn Code G63
Dahlgren VA 22448-5000

Air Weather Service
Attn TechL Lib FL4414 3
Scott AFB IL 62225-5458

GPS Joint Prog Ofc Dir
Attn COL J Clay
2435 Vela Way Ste 1613
Los Angeles AFB CA 90245-5500

Hdqtrs AWS DOO 1
Scott AFB IL 62225-5008

Phillips Lab Atmospheric Sci Div
Geophysics Dirctrt
Attn PL/LYP   Chisholm
Hanscom AFB MA 01731-5000

USAF Rome Lab Tech
Attn Corridor W Ste 262 RL SUL
26 Electr Pkwy Bldg 106
Griffiss AFB NY 13441-4514

USAFETAC DNE
Attn   Glauber
Scott AFB IL 62225-5008

DARPA
Attn B Kaspar
Attn L Stotts
3701 N Fairfax Dr
Arlington VA 22203-1714

NASA Marshal Space Flt Ctr Atmospheric
  Sciences Div
Attn E501   Fichtl
Huntsville AL 35802

NASA Spct Flt Ctr Atmospheric Sciences Div
Attn Code ED 41 1
Huntsville AL 35812

ARL Electromag Group
Attn Campus Mail Code F0250 A Tucker
University of Texas
Austin TX 78712

Univ of Mississippi NCPA
Attn H E Bass
University MS 38577

Dept of Commerce Ctr
Mountain Administration
Attn Sprt Ctr Library R51
325 S Broadway
Boulder CO 80303

Dir for MANPRINT
Ofc of the Deputy Chief of Staff for Prsnnl
Attn J Hiller
The Pentagon Rm 2C733
Washington DC 20301-0300

Natl Ctr for Atmospheric Research
Attn NCAR Library Serials
PO Box 3000
Boulder CO 80307-3000

NCSU
Attn J Davis
PO Box 8208
Raleigh NC 27650-8208

US Army Rsrch Lab
Attn AMSRL-CI-LL Techl Lib (3 copies)
Attn AMSRL-CS-AL-TA Mail & Records
  Mgmt
Attn AMSRL-CS-AL-TP Techl Pub (3 copies)
Attn AMSRL-IS-E Battlefield Environ Div
Attn AMSRL-IS-EE D K Wilson
Attn AMSRL-SE-EE Z G Sztankay
Attn AMSRL-SE-SA N Srour
Adelphi MD 20783-1197

REPORT DOCUMENTATION PAGE			*Form Approved* *OMB No. 0704-0188*
Public reporting burden for this collection of information is estimated to average 1 hour per response, including the time for reviewing instructions, searching existing data sources, gathering and maintaining the data needed, and completing and reviewing the collection of information. Send comments regarding this burden estimate or any other aspect of this collection of information, including suggestions for reducing this burden, to Washington Headquarters Services, Directorate for Information Operations and Reports, 1215 Jefferson Davis Highway, Suite 1204, Arlington, VA 22202-4302, and to the Office of Management and Budget, Paperwork Reduction Project (0704-0188), Washington, DC 20503.			

1. AGENCY USE ONLY *(Leave blank)*	2. REPORT DATE February 1998	3. REPORT TYPE AND DATES COVERED Final, from May to August 1997	

4. TITLE AND SUBTITLE Anisotropic Turbulence Models for Acoustic Propagation Through the Neutral Atmospheric Surface Layer	5. FUNDING NUMBERS DA PR: B53A PE: 61102A
6. AUTHOR(S) David Keith Wilson	

7. PERFORMING ORGANIZATION NAME(S) AND ADDRESS(ES) U.S. Army Research Laboratory Attn: AMSRL-IS-EE (dkwilson@arl.mil) 2800 Powder Mill Road Adelphi, MD 20783-1197	8. PERFORMING ORGANIZATION REPORT NUMBER ARL-TR-1519
9. SPONSORING/MONITORING AGENCY NAME(S) AND ADDRESS(ES) U.S. Army Research Laboratory 2800 Powder Mill Road Adelphi, MD 20783-1197	10. SPONSORING/MONITORING AGENCY REPORT NUMBER

11. SUPPLEMENTARY NOTES AMS code: 61110253A11 ARL PR: 8FEJ60

12a. DISTRIBUTION/AVAILABILITY STATEMENT Approved for public release; distribution unlimited.	12b. DISTRIBUTION CODE

13. ABSTRACT *(Maximum 200 words)*

Several anisotropic models for the three-dimensional spectra of velocity fluctuations in shear-dominated, atmospheric surface-layer turbulence are presented and discussed. These models include a generalized Gaussian model, two forms of generalized von Kármán models; the Kristensen, Lenschow, Kirkegaard, and Courtney model; and the Mann model. The distinction between a "top-down" and "bottom-up" approach to the design of a model is discussed, and how the bottom-up approach generally leads to more satisfactory models is shown. The effects of turbulent anisotropy on acoustic propagation are explored by calculating mutual coherence functions (MCFs) (describing the coherence of a propagating acoustic wave) for the different models. Anisotropy effects have been found that they can be quite significant, even when the separation between the acoustic sensors is small.

14. SUBJECT TERMS Acoustics, atmospheric turbulence, anisotropy			15. NUMBER OF PAGES 77
			16. PRICE CODE

17. SECURITY CLASSIFICATION OF REPORT Unclassified	18. SECURITY CLASSIFICATION OF THIS PAGE Unclassified	19. SECURITY CLASSIFICATION OF ABSTRACT Unclassified	20. LIMITATION OF ABSTRACT UL